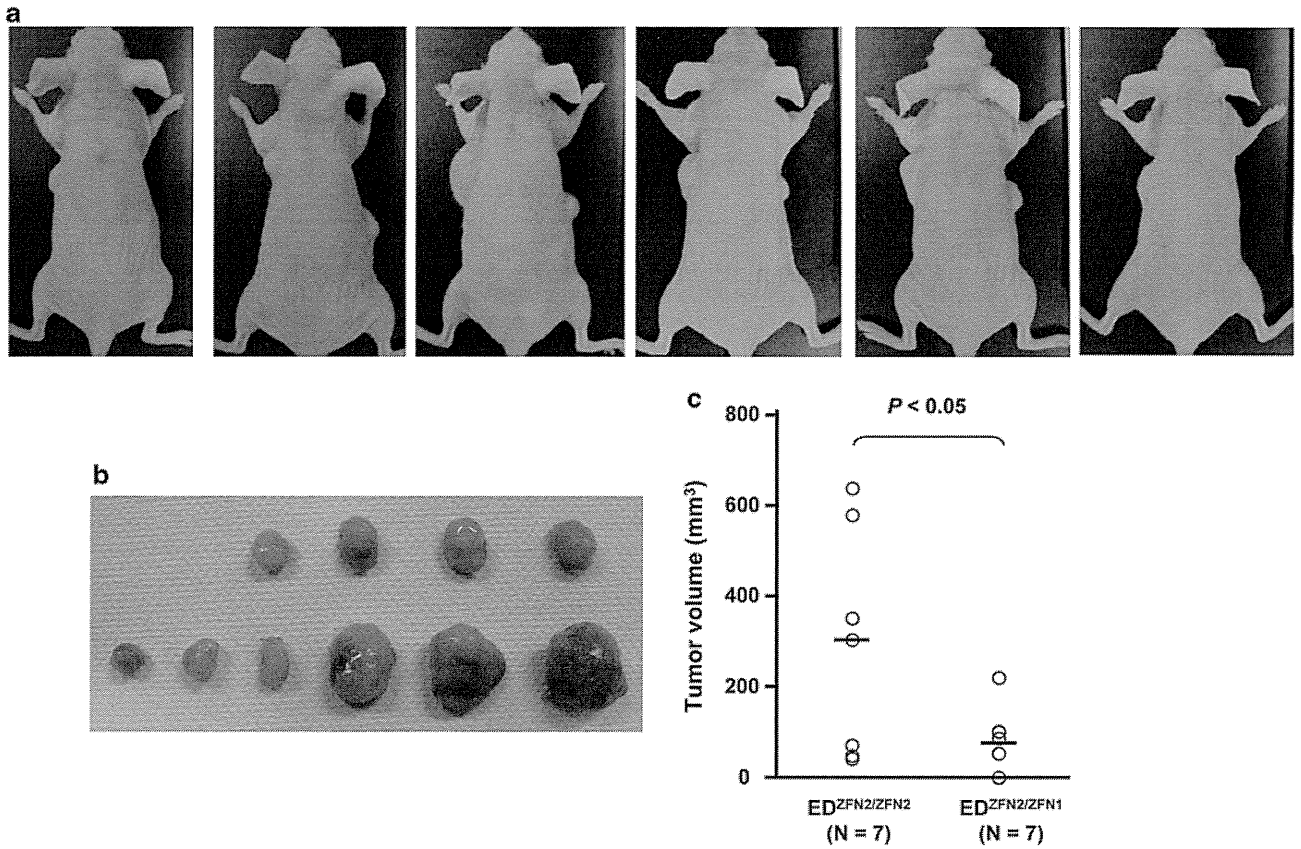

Figure 4. ZFN-mediated inhibition ATL cell tumorigenesis *in vivo*. (**a**) Engraftment of ED cells transduced with ZFNs into Balb/c nude Rag-2/Jak3 double-deficient (nude R/J) mice. $ED^{ZFN2/ZFN1}$ and $ED^{ZFN2/ZFN2}$ cells were transplanted into the left and right flanks, respectively. Mice were photographed at 6 weeks post-cell inoculation. (**b**) Nude R/J mice were killed at 6 weeks post-cell inoculation. The tumors were dissected, photographed and measured. (**c**) The estimated tumor volume is shown. The bar represents the average of the group. Significant differences between the two groups were analyzed using the paired Wilcoxon Rank-Sum test ($P<0.05$).

HTLV-1-transformed cells than in ATL-derived cells. Presumably, this is because HTLV-1-transformed cells are more susceptible to DSB-induced apoptosis.

Next, the physical damage to the LTR sequence caused by ZFN was examined in S1T cell clones recovered from the above experiment. We identified site-specific mutations in 44.1% (15/34 clones) of LTR sequences derived from S1T cell clones, expressing functional ZFN pairs, whereas no mutations were found in LTR clones isolated from the controls (0/7 clones, $P<0.05$; Pearson's exact test, Table 3). Most of the mutations were deletions (average, 14.1 bp/clone). Expression of ZFN3/4 resulted in larger deletions (15.0 bp/clone) than expression of ZFN1/2 (10.2 bp/clone). An insertional mutation was detected only in a single ZFN3/4-transduced clone (2 bp, 2.9%, 1/34 clones; Figures 3b and c). These data suggest that DSB repair occurs in ATL cells, but that the quality of the repair at the ZFN1/2 and ZFN3/4 sites is different. We assume that clones bearing a wild-type LTR might have failed to express ZFNs efficiently, or lost ZFN expression during selection.

The promoter activity of some LTR mutants was examined in a reporter assay in which the reporter plasmid contained both firefly and renilla luciferases, representing positive and negative strand transcription, respectively (Figure 3d–g). The Tax-augmented transcription of the positive strand was reduced by most of the mutations introduced by ZFN1/2 (4/6 clones, Figure 3d). Similarly, the negative strand transcription was also reduced by ZFN1/2-induced mutations (5/6 clones, Figure 3e). On the other hand, increased positive strand transcription was observed in 4/7 LTR mutants recovered from ZFN3/4-transduced cells (Figure 3f). By contrast, many of the LTR mutants showed modestly reduced negative strand transcription (Figure 3g). Sequence analysis suggested that the LTR sequences targeted by ZFNs do not contain binding sites for previously-known transcription factors; therefore, it is possible that the ZFN1/2 target site spans a cis-acting element that supports the efficient transcription of the positive strand. All S1T cell clones were positive for the *gag* gene, suggesting that removal of the entire proviral genome was inefficient, or that ATL cells cannot proliferate without the provirus. However, some S1T cell clones showed reduced gag-to-LTR ratios as measured by quantitative real-time PCR, suggesting that removal of some proviral gene copies is possible (data not shown). Taken together, these data suggest that ZFN-mediated killing of S1T cells is not because of the loss of viral genes, but more likely due to DSB-induced apoptosis.

To evaluate the potential of ZFN1/2 to inhibit tumorigenicity of ATL cells *in vivo*, we adopted ATL cell xenograft model in Balb/c nude Rag-2/Jak3 double-deficient (nude R/J) mice. We chose to use ED cells because they form a tumor mass in nude mice and do not require human interleukin-2 for growth.[18] In addition, ED cells are highly susceptible to infection by MLV vectors. As shown above, the biological effect of ZFN1/2 was greater than that of ZFN3/4 in both HTLV-1-transformed and ATL-derived cell lines. Therefore, we used the ZFN1/2 pair for the *in vivo* study. ED cells constitutively expressing ZFN2 (ED^{ZFN2}) were infected with MLV vectors, harboring *GFP*, *ZFN1* or *ZFN2* gene (Figure 3a). Approximately half of the cells were infected by the MLV vectors as estimated by the number of GFP-positive cells (data not shown). Cells were inoculated intradermally into into nude mice at

2 days post-MLV infection. $ED^{ZFN2/ZFN1}$ cells showed a lower rate of tumor formation, and the tumors were significantly smaller than those in control mice (Paired Wilcoxon Rank-Sum test, $P<0.05$; Figure 4). These data indicate that ZFN1/2 shows promising therapeutic efficacy against ATL.

DISCUSSION

We synthesized two pairs of ZFNs that successfully targeted the HTLV-1 proviral LTR and inhibited the proliferation of HTLV-1-transformed and ATL-derived T-cell lines. ZFN caused physical damage to the LTR and disrupted its function. Even though some cells survived, they contained a defective provirus; therefore, the therapeutic effects should be long-lasting. ZFN was able to remove at least a part of proviral genes from HTLV-1-infected cells and showed anti-tumor effects *in vivo*. Taken together, these data show that ZFN is an attractive therapeutic molecule for treating HTLV-1 infection, and may form the basis of a treatment that eliminates the virus from infected cells. Previous studies used ZFN to edit the human genome.[19,20] However, the work reported herein is unique in that ZFN was used to kill target cells via DSB-triggered apoptosis. This approach can be used for other viruses that establish latent infections and are associated with human malignancies, including retroviruses, Epstein-Barr virus, Kaposi sarcoma herpes virus, papilloma virus and hepatitis B virus.

The choice of a viral vector may improve the efficacy of ZFN in terms of limiting the proliferation of HTLV-1-infected cells. We delivered the *ZFN* gene using an MLV vector; however, adenoviral vectors have been used for the clinical application of ZFNs.[20] The advantage of an adenoviral vector is that it induces transient, but high levels of ZFN expression, whereas retroviral vectors express the gene of interest constitutively, but at low levels. We found that ZFN expression in cells gradually decreased after the long-term cultivation, as is often the case with other genes. This suggests that MLV-mediated gene transduction may not be appropriate for clinical application. We also expect that ZFN-mediated cell killing can be enhanced by inhibiting DSB repair proteins, a method used to increase the efficacy of DNA-damaging agents against tumor cells.[21]

The major hurdle that must be overcome if ZFNs are to be used clinically to treat HTLV-1 infection is their efficient delivery to virus reservoirs. To eliminate HTLV-1 from infected individuals, ZFN must be delivered directly to latently infected cells; however, the latent reservoir of HTLV-1 is poorly understood. Although ZFN has a high-substrate specificity and its non-specific effects are thought to be minimal, delivery of ZFN to all the cells may not be desirable. Cell surface markers of HTLV-1-infected cells, either transformed or not, remain to be identified. We must increase our understanding of HTLV-1 latency if we are to use ZFNs in a clinical setting. Off-target effects are another concern. Although ZFN did not inhibit the proliferation of HTLV-1-negative cells, the risk that ZFNs may edit the human genome must be addressed in future studies. Phase I and II clinical trials using ZFN to treat human immunodeficiency virus infection and recurrent/refractory malignant glioma are currently underway (NCT00842634, 01044654, and 01082926), suggesting that the clinical application of ZFN is feasible. Another issue to be addressed is the stage of HTLV-1 infection at which ZFN should be used; for example, during the latent period or after the onset of HTLV-1-associated disease.

CONFLICT OF INTEREST

The authors declare no conflict of interest.

ACKNOWLEDGEMENTS

This work was supported by the Japan Health Science Foundation, the Japanese Ministry of Health, Labor and Welfare (H23-Shinko-Ippan-028).

AUTHOR CONTRIBUTIONS

AT, ST, EU, RK, KM, SO and JK planned and performed the experiments, and analyzed the data. AT, ST, SO and JK wrote the manuscript.

REFERENCES

1 Nagai M, Osame M. Human T-cell lymphotropic virus type I and neurological diseases. *J Neurovirol* 2003; **9**: 228–235.
2 Watanabe T. HTLV-1-associated diseases. *Int J Hematol* 1997; **66**: 257–278.
3 Yasunaga J, Matsuoka M. Molecular mechanisms of HTLV-1 infection and pathogenesis. *Int J Hematol* 2011; **94**: 435–442.
4 Faris M. Potential for molecular targeted therapy for adult T-cell leukemia/lymphoma. *Int Rev Immunol* 2008; **27**: 71–78.
5 Taylor GP, Matsuoka M. Natural history of adult T-cell leukemia/lymphoma and approaches to therapy. *Oncogene* 2005; **24**: 6047–6057.
6 Carroll D. Progress and prospects: zinc-finger nucleases as gene therapy agents. *Gene Ther* 2008; **15**: 1463–1468.
7 Cannon P, June C. Chemokine receptor 5 knockout strategies. *Curr Opin HIV AIDS* 2011; **6**: 74–79.
8 Handel EM, Cathomen T. Zinc-finger nuclease based genome surgery: it's all about specificity. *Curr Gene Ther* 2011; **11**: 28–37.
9 Onishi M, Kinoshita S, Morikawa Y, Shibuya A, Phillips J, Lanier LL *et al.* Applications of retrovirus-mediated expression cloning. *Exp Hematol* 1996; **24**: 324–329.
10 Kawakami Y, Miura T, Bissonnette R, Hata D, Khan WN, Kitamura T *et al.* Bruton's tyrosine kinase regulates apoptosis and JNK/SAPK kinase activity. *Proc Natl Acad Sci USA* 1997; **94**: 3938–3942.
11 Komano J, Miyauchi K, Matsuda Z, Yamamoto N. Inhibiting the Arp2/3 complex limits infection of both intracellular mature vaccinia virus and primate lentiviruses. *Mol Biol Cell* 2004; **15**: 5197–5207.
12 Shimizu S, Urano E, Futahashi Y, Miyauchi K, Isogai M, Matsuda Z *et al.* Inhibiting lentiviral replication by HEXIM1, a cellular negative regulator of the CDK9/cyclin T complex. *AIDS* 2007; **21**: 575–582.
13 Ono A, Hattori S, Kariya R, Iwanaga S, Taura M, Harada H *et al.* Comparative study of human hematopoietic cell engraftment into BALB/c and C57BL/6 strain of rag-2/jak3 double-deficient mice. *J Biomed Biotechnol* 2011; **2011**: 539748.
14 Attia MA, Weiss DW. Immunology of spontaneous mammary carcinomas in mice. V. Acquired tumor resistance and enhancement in strain A mice infected with mammary tumor virus. *Cancer Res* 1966; **26**: 1787–1800.
15 Harada H, Suzu S, Ito T, Okada S. Selective expansion and engraftment of human CD16+ NK cells in NOD/SCID mice. *Eur J Immunol* 2005; **35**: 3599–3609.
16 Salahuddin SZ, Markham PD, Wong-Staal F, Franchini G, Kalyanaraman VS, Gallo RC. Restricted expression of human T-cell leukemia--lymphoma virus (HTLV) in transformed human umbilical cord blood lymphocytes. *Virology* 1983; **129**: 51–64.
17 Hsu DK, Hammes SR, Kuwabara I, Greene WC, Liu FT. Human T lymphotropic virus-I infection of human T lymphocytes induces expression of the beta-galactoside-binding lectin, galectin-3. *Am J Pathol* 1996; **148**: 1661–1670.
18 Okada M, Maeda M, Tagaya Y, Taniguchi Y, Teshigawara K, Yoshiki T *et al.* TCGF(IL 2)-receptor inducing factor(s). II. Possible role of ATL-derived factor (ADF) on constitutive IL 2 receptor expression of HTLV-I(+) T cell lines. *J Immunol* 1985; **135**: 3995–4003.
19 Perez EE, Wang J, Miller JC, Jouvenot Y, Kim KA, Liu O *et al.* Establishment of HIV-1 resistance in CD4+ T cells by genome editing using zinc-finger nucleases. *Nat Biotechnol* 2008; **26**: 808–816.
20 Holt N, Wang J, Kim K, Friedman G, Wang X, Taupin V *et al.* Human hematopoietic stem/progenitor cells modified by zinc-finger nucleases targeted to CCR5 control HIV-1 *in vivo*. *Nat Biotechnol* 2010; **28**: 839–847.
21 Willmore E, de Caux S, Sunter NJ, Tilby MJ, Jackson GH, Austin CA *et al.* A novel DNA-dependent protein kinase inhibitor, NU7026, potentiates the cytotoxicity of topoisomerase II poisons used in the treatment of leukemia. *Blood* 2004; **103**: 4659–4665.

Supplementary Information accompanies this paper on the Leukemia website (http://www.nature.com/leu)

SCIENTIFIC REPORTS

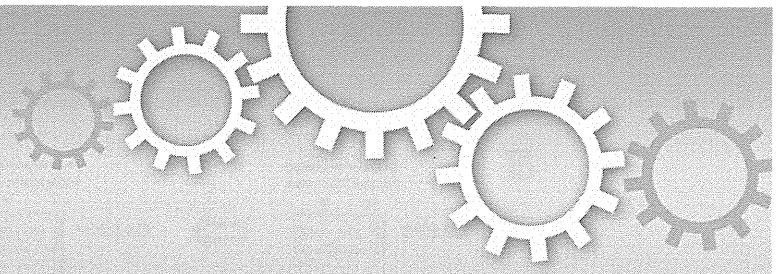

OPEN

SUBJECT AREAS:
MOLECULAR ENGINEERING
GENE THERAPY
VIROLOGY
TUMOUR SUPPRESSORS

Received
30 November 2011

Accepted
12 March 2012

Published
11 April 2012

Correspondence and requests for materials should be addressed to J.K. (ajkomano@nih.go.jp)

Therapeutic potential of HIV protease-activable CASP3

Kosuke Miyauchi, Emiko Urano, Mari Takizawa, Reiko Ichikawa & Jun Komano

AIDS Research Center, National Institute of Infectious Diseases, 1-23-1 Toyama, Shinjuku-ku, Tokyo 162-8640, Japan.

Development of a therapeutic application of CASP3/caspase 3/CPP32, an executor of apoptosis, has been challenging because regulation of its activation is complicated. This study aimed to inhibit cancer cell growth and human immunodeficiency virus type 1 (HIV-1) propagation through a CASP3 mutant, CASP3*, activable by HIV-1-encoded aspartate protease. Active CASP3* was delivered to leukemic cells using a protein transduction vehicle, the lentivirus-like nanoparticle (LENA), which should contain thousands of CASP3*-Gag protein molecules and release the activated CASP3* into the target cell cytoplasm. CASP3*-LENA induced apoptosis in various types of leukemic cells. In addition to being effective against leukemic cells, constitutive expression of CASP3* restricted HIV-1 propagation in SUP-T1 cells. The attenuation of HIV-1 replication in SUP-T1/CASP3* cells was attributed to the elimination of HIV-1-infected cells by apoptosis. These data suggest that CASP3* has therapeutic potential against both lymphoid malignancies and HIV-1 infection.

CASP3 is expressed as an inactive pro-enzyme that is activated upon exposure to apoptosis-inducing stimuli[1,2]. Pro-CASP3 undergoes proteolytic processing by CASP8, 9 and 10 that yields three polypeptides: the pro domain, p17 and p12. The p17 and p12 form a heterodimer that executes the protease activity. CASP3 activates itself as well as CASP6, 7 and 9 by proteolytic cleavage and amplification of the signal for the execution of apoptosis. The therapeutic application of CASP3 is limited because of this complex regulation[3–5]. We overcome this problem by genetic engineering the CASP3.

Here, a mutant of CASP3 designed to be activated specifically by the aspartate protease of human immunodeficiency virus type 1 (HIV-1), but not by other CASPs, was produced (CASP3*) and a proof-of-concept study was conducted to demonstrate the therapeutic potential of CASP3* against lymphoid malignancies and HIV-1 infection.

To achieve leukemic cell killing by CASP3*, a lentivirus-like nanoparticle (LENA) system was utilized[6]. The LENA system is a simple, efficient and reproducible method that we have developed to transduce proteins into mammalian cells[6]. The LENA is different from lentiviral vector in that the former system delivers proteins that are encapsidated into the nanoparticles but not genes as does the latter. Protein transduction does not require *de novo* transcription and translation, and the transferred protein functions immediately after the transduction. Also, LENA is biologically safe since LENA is not an "infectious" agent. Approximately 5,000 CASP3*-Gag proteins are packaged, processed and activated by HIV-1 protease in the particle of LENA. CASP3*-LENA, facilitated by vesicular stomatitis virus G protein (VSV-G), binds to cells and enters them via endocytosis. Membrane fusion between the cell and LENA takes place at the endosome in a VSV-G-dependent manner. The LENA content is then released into the cell cytoplasm. We expected an initiation of apoptosis in CASP3*-LENA-exposed leukemic cells immediately after membrane fusion.

In the HIV/AIDS field, clinical trials have proved that gene therapy approaches are indeed effective against HIV-1 infection[7,8]. However, the emergence of treatment-resistant viruses is problematic, since HIV-1 is a highly mutagenic virus. Also, the "off-target" effect of therapeutic molecules is a serious concern. Thus, developing a highly specific therapeutic gene against HIV-1 provides another option for treatment of HIV-1-infected individuals in a molecular therapy approach.

In this study, the genetically-engineered CASP3 activated specifically by HIV-1 protease was shown to have therapeutic potential against both lymphoid malignancies and HIV-1 infection.

Results

CASP3* has proteolytic cleavage sites for HIV-1 protease adopted from the matrix (MA or $p17^{MA}$)-capsid (CA or $p24^{CA}$) junction of HIV-1 $Pr55^{Gag}$ (Gag, Fig. 1a). The myristoylation signal of Lyn was attached at the

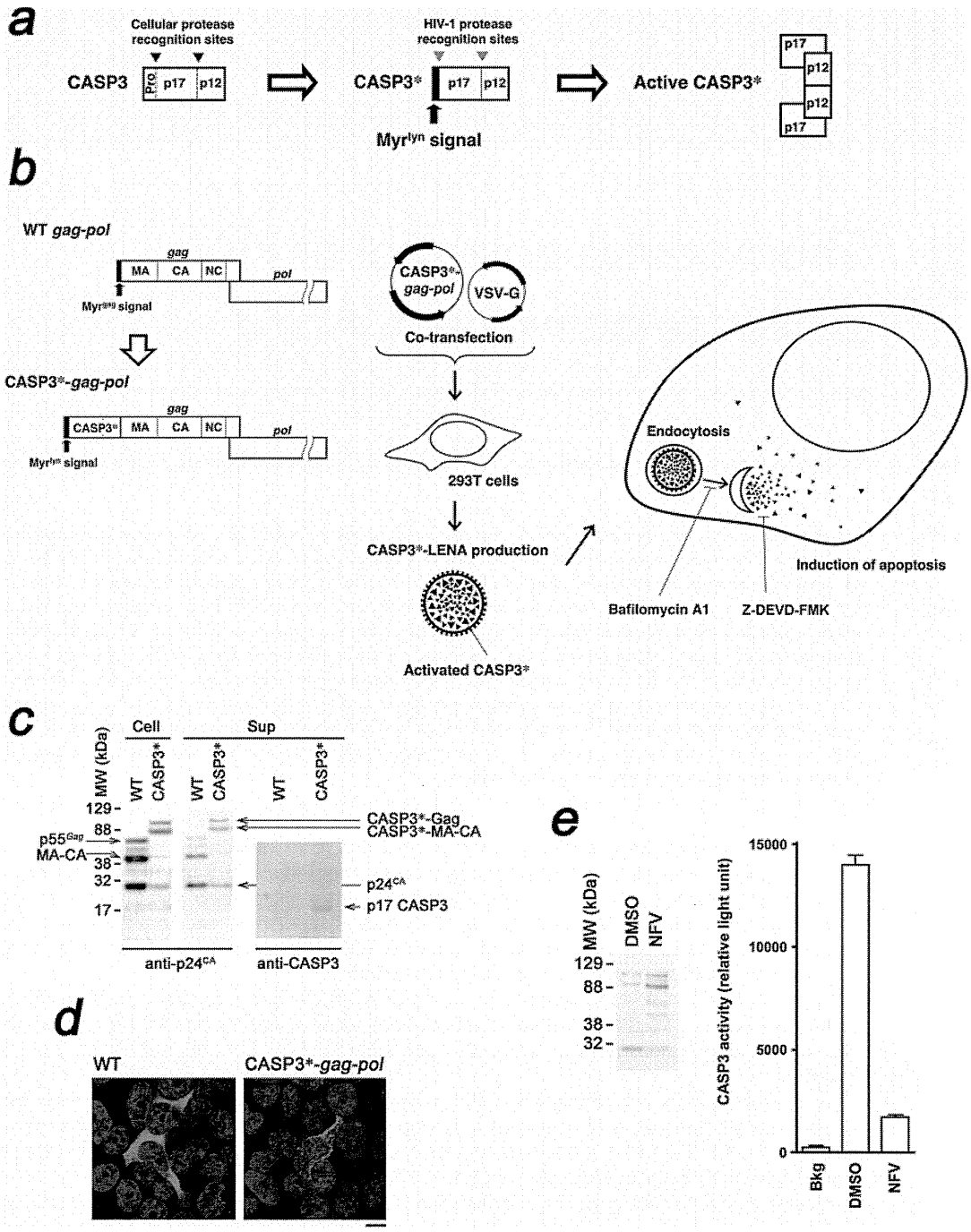

Figure 1 | Construction, production and characterization of CASP3*-LENA. (a) Genetic structure of CASP3 and the genetic modification to produce HIV-1 protease-activable CASP3*. The cellular (gray triangle, digesting D28-S29 and D175-S176 junctions) and HIV-1 (black triangle) protease proteolytic sites are indicated. The CASP3 D28 was replaced with amino acids 127–136 (VSQNYPIVQ) from HIV-1 Gag (according to the HXB2 coordinate). The amino acids 129–134 (QNYPIV) from HIV-1 Gag according to the HXB2 coordinate was inserted after CASP3 D175. HIV-1 protease targets the YP junction. The enzyme is active when the p17 and p12 subunits are dimerized. (b) Production of CASP3*-LENA and its mechanism of action. The *CASP3** was placed at the 5' end of wild type (WT) *gag-pol* to yield CASP3*-*gag-pol*. The proteolytic cleavage sites within Gag for HIV-1 protease and the proteolytic products are indicated MA, matrix; CA, capsid; and NC, nucleocapsid. The CASP3*-*gag-pol* and VSV-G expression vectors were co-transfected into 293T cells. Then, the VSV-G-encapsidated LENA containing activated CASP3* protein was produced in the culture supernatant. CASP3*-LENA enters cells via an endocytotic route, with the content released from endosomes at the site of membrane fusion. The action points of Bafilomycin A1 (BAF) and the CASP3 inhibitor Z-DEVD-FMK are indicated. (c) Expression of CASP3*-gag-pol and CASP3*-LENA production. The cell lysates (Cell) and culture supernatants (Sup) of 293T cells transfected with either wild type (WT) or CASP3*-gag-pol (CASP3*) expression vector were analyzed by Western Blot. The corresponding protein for each band is indicated. (d) Immunofluorescence assay showing the distribution of WT Gag or CASP3*-Gag (CASP3*) in 293T cells transfected with either WT or CASP3*-*gag-pol* (CASP3*) expression vector. Red and blue represent the anti-$p24^{CA}$ monoclonal antibody-stained signal and the Hoechst 33258-stained nucleus, respectively. Magnification, x630; scale bar, 10 μm. (e) Detection of CASP3 enzyme activity in purified CASP3*-LENA. CASP3*-LENA was produced either in the presence or absence of nelfinavir (NFV) and collected by ultracentrifugation over a 20% sucrose layer. DMSO was used as a control. The amount of CASP3*-LENA and the cleavage pattern of Gag were examined by Western blot (left). CASP3 enzyme activity was detected in the CASP3*-LENA lysate (right).

amino-terminus and serves as a membrane-targeting signal. The pro domain of CASP3 was dispensable for enzyme activity and was removed from this construct. Then, the CASP3* was applied to the LENA system for the leukemic cell killing experiment (Fig. 1b). The CASP3*-Gag and its proteolytic products were detected in the 293T cell lysate transfected with pCASP3*-*gag-pol* by Western blot analysis (Fig. 1c, Cell) in a pattern similar to that of wild-type Gag-pol (WT, Fig. 1c). However the processing efficiency of Gag was slightly attenuated in the CASP3* construct compared with WT, as highlighted by the smaller amount of $p24^{CA}$ relative to its precursor. In the culture supernatant of transfected 293T cells, CASP3*-LENA was detected by Western blot analysis (Fig. 1c, Sup). The presence of CASP* was verified by Western blot analysis using anti-CASP3 antibody that specifically recognizes the p17 subunit of CASP3 (Fig. 1c, Sup). In 293T cells transiently transfected with the WT expression plasmid, Gag was evenly distributed in the cell cytoplasm as visualized by an immunofluorescence assay (Fig. 1d). In contrast, CASP3*-Gag was distributed mainly in the cytoplasm and, to a lesser extent, in the nucleus, forming numerous fine aggregations (Fig. 1d). Also, some CASP3*-Gag signal was detected at the cell periphery (Fig. 1d). Despite these differences, LENA production by CASP3*-Gag-pol was as efficient as that by WT; the signal ratio of CASP3*-Gag and its proteolytic products in the virus-like particle (VLP) fraction relative to the cell lysate were comparable to that of the WT (Fig.1c).

To verify the enzyme activity of CASP3* in LENA, the proteolytic activity of CASP3* was measured using a caspase 3/7-specific substrate, DEVD-aminoluciferin, that luminesces upon cleavage. Significant enzymatic activity was detected in the purified CASP3*-LENA (Fig. 1e). Importantly, this signal was substantially reduced when proteolytic cleavage of CASP3*-Gag was attenuated through the preparation of CASP3*-LENA in the presence of 0.5 μM HIV-1 protease inhibitor nelfinavir (NFV; Fig. 1e). These data suggest that active CASP3* is enveloped in the LENA and that the activation of CASP3* is dependent on HIV-1 protease.

HIV-1 protease is fully activated after viral budding. Thus, the majority of CASP3* should be activated outside cells. This minimizes damage to LENA-producing cells by CASP3*. However, LENA-producing 293T cells were damaged upon Gag-pol expression presumably due to the cytotoxicity of the small amount of HIV-1 protease activated in the cell cytoplasm upon overexpression of the protein. Cell viability and LENA production improved when the LENA-producing cells were treated with a low dose of HIV-1 protease inhibitor. Preparation of LENA in the presence of 0.2 μM saquinavir (SQV) increased the LENA yield by approximately 4-fold (Fig. 2a). Under these conditions, HIV-1 protease in LENA remained active as evidenced by the production of cleavage intermediates of CASP3*-Gag (Fig. 2a). The activation of CASP3* was not blocked under these conditions because a cleavage intermediate, MA-CA, predicated the release of CASP3* from the precursor (Fig. 2a, arrowhead), and the biological activity of CASP3*-LENA was detected as described below. Similar data were obtained using the low dose of NFV.

For leukemic cell killing by CASP3*-LENA, an acute T cell lymphoblastic leukemia (ALL) cell line, MOLT-4, was chosen. MOLT-4 cell viability was significantly attenuated when cells were exposed to CASP3*-LENA, whereas no cell killing was observed in WT-LENA or non-enveloped CASP3*-LENA at 1d post-LENA exposure (Fig. 2b and 2c). A cell metabolism-based cell viability assay revealed that 93.3% of cell viability was lost in CASP3*-LENA-exposed MOLT-4 cells at 1d post-LENA exposure (Fig. 2b). This cell killing was more efficient when cells were treated with CASP3*-LENA prepared in the presence of 0.2 μM SQV bearing a higher LENA titer (99.2%, Fig. 2b). The MOLT-4 cells exposed to CASP3*-LENA contained fragmented nuclei with condensed chromatin, characteristic of cells undergoing apoptosis (Fig. 2d). Such nuclear morphology was not found in MOLT-4 cells exposed to WT-LENA or non-enveloped CASP3*-LENA. Induction of apoptotic cell death was detected at 6 h post-LENA exposure by Annexin V staining (Fig. 2e). The VSV-G functional inhibitor Bafilomycin A1, which prevents the endosome acidification required for the activation of VSV-G, rescued the cells from apoptotic cell death at 12.5 ng ml^{-1} (Fig. 2c-f). A cell-permeable CASP3 inhibitor, Z-DEVD-FMK, also protected cells from CASP3*-LENA-induced apoptosis at 0.5 μM (Fig. 2c–g). These data suggest that the cell death induced by CASP3*-LENA is dependent on VSV-G function and the proteolytic function of CASP3*. The death inducing titer of CASP3*-LENA for MOLT-4 cell was 2.0×10^6 particles per milliliter, which was estimated from the dose-dependent cell killing kinetics using serially diluted CASP3*-LENA preparations (average of four independent experiments).

In addition to MOLT-4 cells, CASP3*-LENA induced apoptosis in two more leukemic cell models, SUP-T1 cells, a pleural effusion T cell lymphoblastic lymphoma cell line, and the HTLV-1-transformed T cell line M8166, a model for adult T cell leukemia (ATL, Fig. 2g). Similar data were obtained in the human chronic myelogenous leukemia (CML)-derived cell line K562 and the neuroblastoma cell line NP-2 (data not shown). These data indicate that the cell killing activity of CASP3*-LENA is not restricted to the leukemic cells. In these experiments, WT-LENA and non-enveloped CASP3*-LENA failed to induce apoptosis. These data demonstrate the attractiveness of CASP3* protein transduction by LENA as a tool for molecular cancer therapy. The cell killing activity of CASP3*-LENA was not detected in primary blood mononuclear cells (data not shown). This is presumably because the primary cells are inefficient to the LENA-mediated protein delivery and/or to the CASP3-induced apoptosis, or both. This suggests that the CASP3*-LENA may favor cancer cells to induce apoptotic cell death.

CASP3* was also applied to limit HIV-1 replication. We hypothesized that CASP3*-expressing T cells may be more susceptible to apoptosis upon HIV-1 infection due to the expression of HIV-1 protease in infected cells. To this end, SUP-T1 cells were transduced with CASP3* using a murine leukemia virus (MLV) vector, and two independently isolated pairs of SUP-T1 cells were analyzed (Fig. 3a). The rate of cell proliferation and the susceptibility to apoptosis induced by a serim depriviation in SUP-T1/CASP3* cells were indistinguishable from those in SUP-T1/Cont cells (data not shown). Cells were exposed to a low- or high-dose HIV-1 preparation and viral replication was monitored. In both isolates, HIV-1 propagation in SUP-T1/CASP3* cells was attenuated regardless of the HIV-1 exposure dose (Fig. 3b). These data suggest that CASP3* can limit the propagation of HIV-1 in tissue culture.

To determine the mechanism by which HIV-1 replication is blocked, the viral entry phase and the production phase were investigated separately. If the virus-associated protease is responsible for the activation of CASP3* at the viral entry phase, infection with the HIV-1-based lentiviral vector should also kill SUP-T1/CASP3* cells. Thus, the establishment efficiency of lentiviral vector infection in SUP-T1/CASP3* cells should be lower than that in control cells. To test this, SUP-T1/CASP3* cells were infected with a lentiviral vector expressing luciferase upon establishment of infection. The luciferase activity in SUP-T1/CASP3* cells at 4 d post-infection was lower than in the control cells (Fig. 3c). On the other hand, the levels of MLV-transduced luciferase activity in SUP-T1/CASP3* cells were similar to those in the control cells (Fig. 3c). Note that CASP3* was not activated by MLV since the substrate preference of MLV protease is distinct from that of HIV-1 protease. These data suggest that virus-associated HIV-1 protease is capable of activating CASP3* to induce apoptosis in SUP-T1/CASP3* cells. Luciferase activity was still detected in the lentiviral vector-infected SUP-T1/CASP3* cells (Fig. 3c), implying that some cells might have lost the high-level expression of CASP3* or a single virion-associated

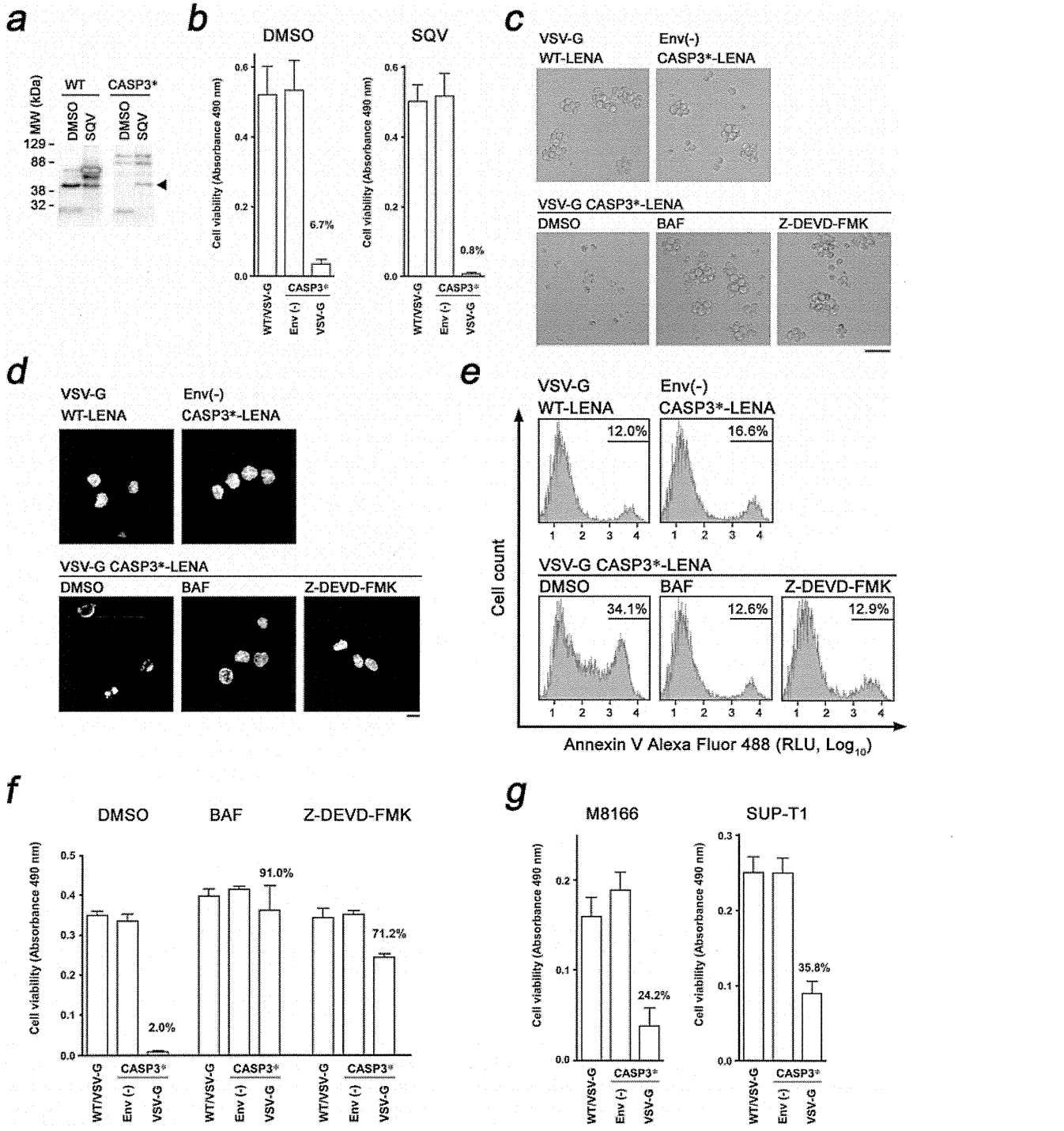

Figure 2 | Induction of apoptosis in leukemic cells by CASP3*-LENA. (a) Enhancement of WT- and CASP3*-LENA production by a low dose of saquinavir (SQV, 0.2 μM). DMSO was used as a solvent control. The arrowhead indicates a signal representing the MA-CA, indicating the release of CASP3* from CASP3*-Gag. (b) Quantitative analysis of MOLT-4 cell viability after LENA exposure. Cell viability was scored by colorimetric assay at 1d post-LENA exposure comparing WT-LENA encapsidated with VSV-G (WT/VSV-G), non-enveloped CASP3*-LENA (ENV(-)), and CASP3*-LENA encapsidated with VSV-G. The average and standard deviation from triplicated wells using LENA produced in the presence or absence of SQV are shown (SQV and DMSO, respectively). (c) Light microscopic observation of MOLT-4 cells treated with LENA produced in the presence of low-dose SQV. Cells were imaged at 1 d post-LENA exposure. Cells were treated with either Bafilomycin A1 (BAF) or the CASP3 inhibitor Z-DEVD-FMK. DMSO was used as a solvent control. Bar, 50 μm; magnification x100. (d) Nuclear morphology of MOLT-4 cells treated with LENA produced in the presence of low-dose SQV. Cells were imaged at 1 d post-LENA exposure after staining with Hoechst dye. Cells were treated with either BAF or Z-DEVD-FMK. DMSO was used as a solvent control. Bar, 10 μm; magnification x630. (e) Flow cytometric detection of apoptotic MOLT-4 cells. Cells were stained with Annexin V Alexa Fluor 488 at 6 h post-exposure to LENA produced in the presence of low dose nelfinavir (NFV, 0.2 μM). The live cell fraction was gated to analyze the early phase of apoptotic cell death. Cells were treated with either BAF or Z-DEVD-FMK. DMSO was used as a solvent control. RLU, relative light units. (f) Quantitative analysis of MOLT-4 cell viability after exposure to LENA produced in the presence of low-dose NFV (0.2 μM). Cell viability was scored at 1d post-LENA exposure. Cells were treated with either BAF or Z-DEVD-FMK. DMSO was used as a solvent control. (g) Quantitative analysis of M8166 and SUP-T1 cell viabilities as perfomed on MOLT-4 cells.

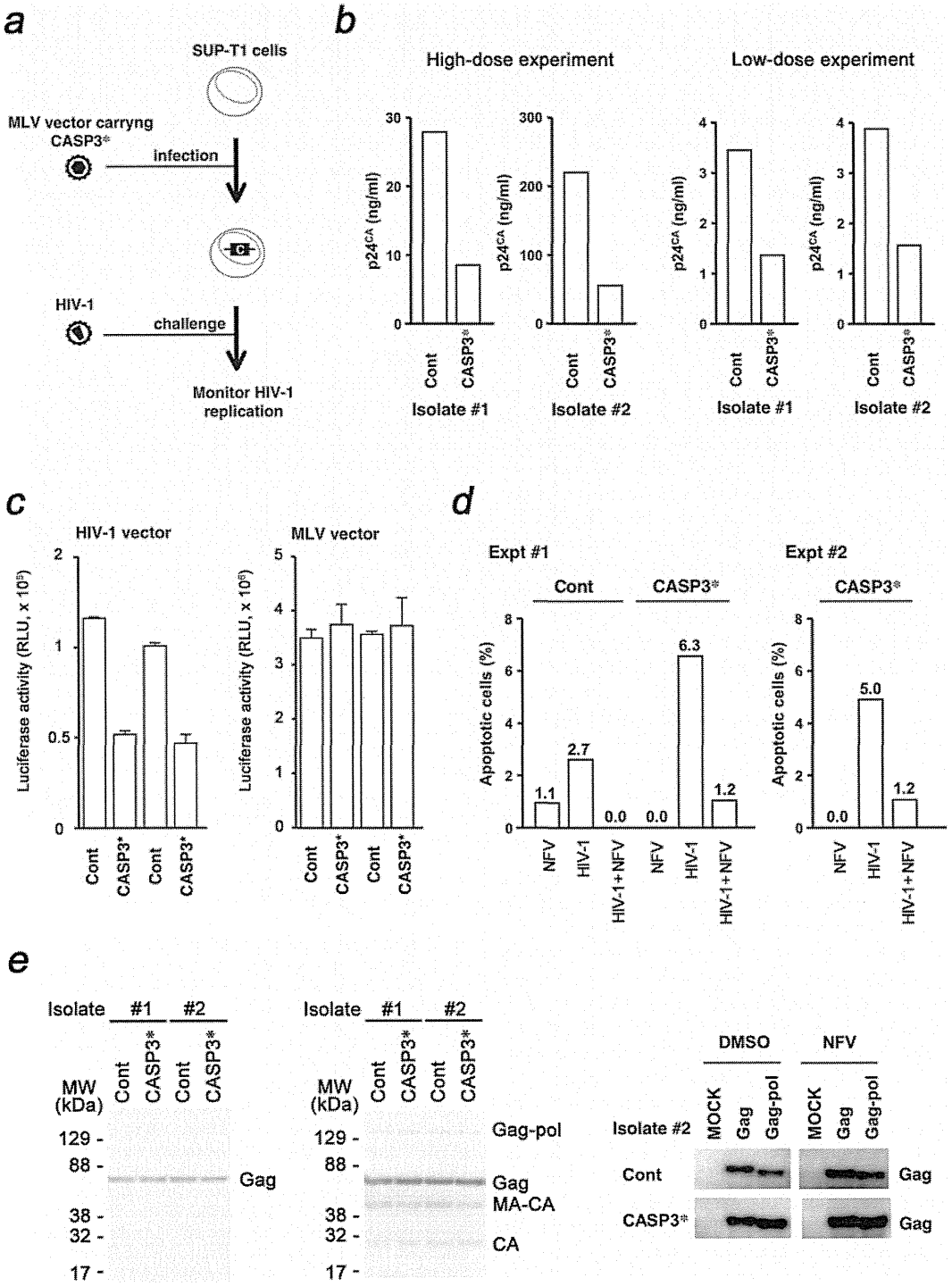

Figure 3 | Inhibition of HIV-1 propagation by CASP3*. (a) Schematic representation of the experimental approach. SUP-T1 cells were infected with MLV carrying the *CASP3** to produce cells constitutively expressing CASP3*. These cells were infected with HIV-1, and the replication efficiency of HIV-1 was measured using viral $p24^{CA}$ antigen in the cell culture medium. (b) Inhibition of $HIV\text{-}1_{NL4\text{-}3}$ replication in SUP-T1/CASP3* cells. Cells were exposed to high- or low-dose viral preparation yielding 25 ng or 1.3 ng of $p24^{CA}$ per 1×10^5 cells, respectively. The viral $p24^{CA}$ concentration in the culture supernatant was measured at 6–9 d post-viral infection. Results shown were obtained from two independent isolates of SUP-T1/CASP3* and control cells. (c) Analysis of SUP-T1/CASP3* cell fate after HIV-1 entry. Luciferase activity of cells infected with either an HIV-1-based lentiviral vector or an MLV vector was measured at 4 d post-infection. RLU, relative light units. (d) Flow cytometric detection of apoptotic SUP-T1/Cont and SUP-T1/CASP3* cells by $HIV\text{-}1_{NL4\text{-}3}$ infection. The percentage of Annexin V Alexa Fluor 488 positive cells was measured at 6 h post-nelfinavir (NFV) exposure, post-HIV-1 infection, and post-HIV-1 infection in the presence of 2 μM NFV, and subtracted from the percentage of Annexin V positive cells in untreated controls. The live cell fraction was gated according to scatter to analyze the early phase of apoptotic cell death. Data from two independent experiments are shown. For this experiment, cells from isolate #2 were used. (e) Analysis of SUP-T1/CASP3* cell fate upon HIV-1 production. The SUP-T1/CASP3* cells were transduced with HIV-1 Gag-pol or Gag by either MLV vector (left panel) or transfection (right panel), and the expression of transduced proteins was detected at 7 d post-gene transduction by Western blot. For the transfection experiment, cells were maintained in the presence of 0.5 μM NFV to detect the effect of Pol on cell survival.

protease might not be able to initiate CASP3* activation at levels sufficient to kill all of the infected cells. Next, the induction of apoptosis by the virion-associated viral protease was examined directly. SUP-T1/CASP3* cells were exposed to HIV-1 and the cells were probed with Annexin V. At 6 h post-infection, 2.7% of SUP-T1/Cont cells underwent apoptosis, which was lowered by NFV (Fig. 3d), suggesting that the HIV-1 infection induces apoptotic cell death in a HIV-1 protease-dependent manner as previously reported[9,10]. By contrast, the apoptotic cells was detected more frequently in SUP-T1/CASP3* cells than in SUP-T1/Cont cells (6.3% and 5.0% in two independent experiments), which was drastically decreased to 1.2% in the presence of NFV (Fig. 3d). These data suggest that the CASP3* predispose cells to undergo apoptosis upon HIV-1 infection, and the virus-associated protease is responsible for the induction of apoptosis.

To examine the viral production phase, the HIV-1 *gag-pol* was transduced into SUP-T1/CASP3* cells by MLV vector, and the levels of Gag were evaluated. If HIV-1 protease activity in virus producing cells is responsible for the activation of CASP3*, then the expression of Gag-pol, not Gag, should confer the cell growth disadvantage, resulting in reduced levels of Gag in these cells. Transfected SUP-T1/CASP3* cells were subjected to Western Blot analysis at 7 d post-infection. The levels of Gag and its proteolytic products in SUP-T1/CASP3* cells were indistinguishable from those of the control cells (Fig. 3e). Similar results were obtained when SUP-T1/CASP3* cells were transfected with a plasmid expressing HIV-1 Gag-pol (Fig. 3e). These data indicate that the attenuation of HIV-1 replication in SUP-T1/CASP3* cells is due to the activation of CASP3* by virion-associated HIV-1 protease at the viral entry phase, leading to the depletion of virus-infected cells from the culture by apoptosis. In agreement with this model, the inhibition of apoptosis by Z-DEVD-FMK enhanced the efficiency of HIV-1 replication (data not shown).

Discussion

This study provides evidence that CASP3* has therapeutic potential against cancer and HIV-1 infection, overcoming the potential difficulty of CASP3 for the application to human gene therapy[3,4,11]. The cancer therapy by CASP3*-LENA may be more applicable to solid tumors due to the current technological limit in particle delivery. However, to apply the CASP3*-LENA approach to the cancer therapy, it is critical to improve the potency of CASP3*-LENA. This is because the cell killing activities of CASP3*-LENA in some transformed cells, including MT-4, a HTLV-1-transformed human T cell line, were undetectable although the LENA-mediated protein delivery by LENA has been shown to be highly efficient in MT-4 cells[6]. MT-4 cells are highly resistant to apoptosis because they express potent anti-apoptotic genes, such as HTLV-1 Tax[12–14]. The Tax induces expression of intracellular caspase inhibitor, cFLIP, which inhibits the activation cycle of CASPs[15,16]. Cancer cells often express high levels of cellular inhibitor of apoptosis protein (CIAP), which may lower the susceptibility of cells to apoptosis induced by CASP3. We may be able to overcome this issue by generating a CASP3* mutant that does not interact with CIAP. The potentiation of CASP3*-LENA should also contribute to reduce the number of injections necessary to achieve the therapeutic effect. Additionally, for clinical applications, a regulatory system to control the cell tropism of LENA needs to be developed.

For HIV-1 infection, CASP3* may be applicable to adoptive stem cell therapy, alternatively termed intracellular vaccination. Stem cell gene therapy has been shown to be effective in clinical trials against HIV-1 infection, as has shRNA therapy targeting CCR5 mRNA[7]. Gene therapy using a zinc finger nuclease was found to be effective against HIV-1 infection as well[8]. These therapeutic approaches target nucleic acids, and off-target effects represent a serious concern. CASP3* is designed to be activated specifically by HIV-1 protease; thus, it offers a basis for a novel therapeutic approach with few "off-target" effects. CASP3* induces suicide in HIV-1-infected cells, and does not yield latently-infected cells. The CASP3* approach should be effective against drug-resistant HIV-1 strains since the anti-viral mechanism of CASP3* is distinct from those of currently-available anti-retroviral drugs. Furthermore, a CASP3*-resistant HIV-1 may not emerge easily. This is because mutations in viral protease that do not affect Gag processing but also do not activate CASP3* are unlikely to occur. Additionally, our strategy is applicable to other infectious diseases if the infectious agents encode proteases with unique substrate preferences. In summary, our work provides a platform for the development of a CASP3*-based therapy against cancer and HIV-1 infection.

Methods

Plasmids. *CASP3* was amplified from MT-4 total RNA using a two-step PCR protocol. For the first reaction, two RT-PCR reactions were performed using the following primer sets: fwd #1 5'-acc ggt cAG CCA GAA CTA Ccc cat cgt gca gTC Tgg aat atc cct gga caa c-3' and rev #1 5'-CTc acg atg ggG TAG TTC TGg tct gtc tca atg cca cag tc-3'; and fwd #2 5'-acC AGA ACT ACc cca tcg tgA GTG GTG TTG ATG ATG ACA TGG-3' and rev #2 5'-CAA TTG GTG ATA AAA ATA GAG TTC TTT TG-3'. The second PCR reaction was performed using fwd #1 and rev #2 primers targeting the products obtained in the first RT-PCR reactions. The *AgeI-MfeI* fragment of the PCR product was cloned into *AgeI-EcoRI* sites of p*lyn*MyGFP-*gag-pol*[6], generating pCASP3*-*gag-pol*. The retroviral expression vector pQcCASP3* was constructed by amplifying *CASP3** by PCR as detailed above using 5'-acc ggt gcc acc ATG ggc TCT gga ata tcc ctg gac aac-3' and 5'-CAA TTG TTA GTG ATA AAA ATA GAG TTC TTT TG-3', and cloned into *AgeI-EcoRI* sites of pQcXIP (Clontech, Palo Alto, CA). The pCMMP Gagf vector was constructed by cloning a *XhoI-BamHI* fragment from pGag-GFP[17] into the corresponding restriction sites of pCMMP KRAB[18]. The pCMMP HIV-1 *gag-pol* IRES GFP was constructed by three step cloning. First, the *AgeI-BamHI* KRAB gene fragment from pCMMP KRAB was cloned into the corresponding restriction sites of pCMMP LacZ IRES GFP[9], generating pCMMP KRAB IRES GFP. The *AgeI-EcoRI BlaM* gene fragment amplified from pUC19 by PCR[6] was cloned into the *AgeI-MfeI* sites of pCMMP KRAB IRES GFP, generating pCMMP BlaM IRES GFP. The *EcoRI-XhoI* HIV-1 *gag-pol* gene fragment from p*gag-pol*[18] was cloned into the corresponding restriction sites of pCMMP BlaM IRES GFP, generating pCMMP HIV-1 *gag-pol* IRES GFP. The HIV-1 proviral DNA pNL4-3 was obtained from the NIH AIDS Research and Reference Program. The HIV-1 Gag expression vector pHIV-1 Gagf was produced by cloning an *AgeI-BamHI* fragment from pHIV-1 Gagf-GFP[17] into the corresponding sites of pEGFP-C2 (Clontech).

Cells, viability assay, and transfection. Cells were maintained in RPMI 1640 medium (Sigma, St. Louis, MA) supplemented with 10% fetal bovine serum (Japan Bioserum, Tokyo), 100 U ml^{-1} penicillin, and 100 μg ml^{-1} streptomycin (Invitrogen), at 37°C in a humidified 5% CO_2 atmosphere. Cells were transfected with Lipofectamine 2000 according to the manufacturer's protocol (Invitrogen). Bafilomycin A1 was used at a concentration of 12.5 ng ml^{-1} (Sigma), and a CASP3 inhibitor, Z-DEVD-FMK, was used at a concentration of 0.5 μM (BioVision, Mountain View, CA). The HIV-1 protease inhibitors nelfinavir (NFV) and saquinavir (SQV) were obtained from the NIH AIDS Research and Reference Reagent Program. To produce VSV-G-pseudotyped LENA, 200 ng pVSV-G (Clontech) and 2 μg pCASP3*-gag-pol or *pgag-pol*[18] were transfected into 293T cells. Non-enveloped LENA was produced using pcDNA3 (Invitrogen) in place of pVSV-G. The LENA preparation was passed through nitrocellulose filters (0.45 μm). Cell viability was scored by the CellTiter 96 Aqueous One Solution Cell Proliferation Assay (Promega). For the transfection of plasmids into SUP-T1 cells, a DEAE-dextran protocol was employed. Five million cells were resuspended in 250 μl of STBS (25 mM TrisCl, pH 7.4, 137 mM NaCl, 5 mM KCl, 0.6 mM Na_2HPO_4, 0.7 mM $CaCl_2$, and 0.5 mM $MgCl_2$), including 10 μg of plasmid DNA. Cells were mixed with 250 μl of STBS containing 1 mg ml^{-1} of DEAE-dextran and incubated for 30 min at room temperature (RT). The cells were then incubated with STBS containing 10% DMSO for 2 min at RT and washed with 1 ml HBSS (Invitrogen).

Protein transduction. Protein transduction was performed as described previously by incubating approximately 1×10^6 cells with 1 ml LENA-containing culture medium at 37°C[3].

Immunological detection. The detection of viral gene products by Western blot analysis was performed as described previously[19], except that the anti-$p24^{CA}$ monoclonal antibody clone 183-H12-5C and anti-CASP3 p17 subunit polyclonal antibody (Cat. # AB3623, Millipore, Tokyo, Japan) were used. Immunofluorescent analysis was performed as described previously using the same monoclonal antibody[18]. Signals were detected using an LAS-3000 mini Lumino-Image analyzer operated by the LAS-300mini Image Reader software (ver.2.2, Fuji Film, Tokyo, Japan). The brightness and contrast of the image were adjusted using Adobe Photoshop (ver.7.0, Adobe, Tokyo, Japan).

Microscopy. Cells were imaged by confocal fluorescence microscopy (LSM510 Meta, Carl Zeiss MicroImaging Inc., Tokyo, Japan). For the imaging of nuclei, multiple focal planes were projected to generate a single image.

Virus production and infection. The HIV-1, lentiviral and MLV vectors used have been described previously[9]. The pQcXIP was used as a control for pQcCASP3*.

Detection of CASP3 enzymatic activity. The substrate for the CASP3 enzyme assay was purchased from Promega (Caspase-Glo 3/7 Assay System, Promega, Madison, WI). Luciferase activity was measured using the Steady-Glo Luciferase Assay system (Promega). Luminescence was detected using a Veritas™ Microplate Luminometer (Promega).

Annexin V apoptosis assay. Cells were analyzed by flow cytometry using the Vybrant Apoptosis Assay kit (Invitrogen).

Enzyme-Linked Immunosorbent Assay (ELISA). A p24 ELISA was conducted according to the manufacturer's protocol (Zeptometrics, Buffalo, NY). To measure cellular p24, transfected 293T cells were washed once with PBS, lysed in 500 µl buffer A (described above) for 30 min, and then subjected to the ELISA.

1. Cohen, G. M. Caspases: the executioners of apoptosis. *Biochem J.* **326**, 1–16 (1997).
2. Boatright, K. M. & Salvesen, G. S. Mechanisms of caspase activation. *Curr Opin Cell Biol.* **15**, 725–31 (2003).
3. Yamabe, K. *et al.* Cancer gene therapy using a pro-apoptotic gene, caspase-3. *Gene Ther.* **6**, 1952–9 (1999).
4. Cam, L., Boucquey, A., Coulomb-L'hermine, A., Weber, A. & Horellou, P. Gene transfer of constitutively active caspase-3 induces apoptosis in a human hepatoma cell line. *J Gene Med.* **7**, 30–8 (2005).
5. Walters, J. *et al.* A constitutively active and uninhibitable caspase-3 zymogen efficiently induces apoptosis. *Biochem J.* **424**, 335–45 (2009).
6. Aoki, T., Miyauchi, K., Urano, E., Ichikawa, R. & Komano, J. Protein transduction by pseudotyped lentivirus-like nanoparticles. *Gene Ther* **18**, 936–941 (2011).
7. Mitsuyasu, R. T. *et al.* Phase 2 gene therapy trial of an anti-HIV ribozyme in autologous CD34+ cells. *Nat Med.* **15**, 285–92. Epub 2009 Feb 15. (2009).
8. Holt, N. *et al.* Human hematopoietic stem/progenitor cells modified by zinc-finger nucleases targeted to CCR5 control HIV-1 in vivo. *Nat* **28**, 839–47 (2010).
9. Komano, J., Miyauchi, K., Matsuda, Z. & Yamamoto, N. Inhibiting the Arp2/3 complex limits infection of both intracellular mature vaccinia virus and primate lentiviruses. *Mol Biol Cell.* **15**, 5197–207. Epub 2004 Sep 22. (2004).
10. Nicholson, D. W. *et al.* Identification and inhibition of the ICE/CED-3 protease necessary for mammalian apoptosis. *Nature.* **376**, 37–43 (1995).
11. Wagner, R. *et al.* Rev-independent expression of synthetic gag-pol genes of human immunodeficiency virus type 1 and simian immunodeficiency virus: implications for the safety of lentiviral vectors. *Hum Gene Ther* **11**, 2403–13 (2000).
12. Shaulian, E. & Karin, M. AP-1 as a regulator of cell life and death. *Nat Cell Biol.* **4**, E131-6 (2002).
13. Azran, I., Schavinsky-Khrapunsky, Y. & Aboud, M. Role of Tax protein in human T-cell leukemia virus type-I leukemogenicity. *Retrovirology.* **1**, 20 (2004).
14. Charoenthongtrakul, S., Zhou, Q., Shembade, N., Harhaj, N. S. & Harhaj, E. W. Human T cell leukemia virus type 1 Tax inhibits innate antiviral signaling via NF-kappaB-dependent induction of SOCS1. *J Virol.* **85**, 6955–62. Epub 2011 May 18. (2011).
15. Krueger, A. *et al.* HTLV-1 Tax protects against CD95-mediated apoptosis by induction of the cellular FLICE-inhibitory protein (c-FLIP). *Blood.* **107**, 3933–9. Epub 2006 Jan 10 (2006).
16. Okamoto, K., Fujisawa, J., Reth, M. & Yonehara, S. Human T-cell leukemia virus type-I oncoprotein Tax inhibits Fas-mediated apoptosis by inducing cellular FLIP through activation of NF-kappaB. *Genes Cells.* **11**, 177–91 (2006).
17. Aoki, T. *et al.* Improvement of lentiviral vector-mediated gene transduction by genetic engineering of the structural protein Pr55 Gag. *Gene Ther* **17**, 1124–33 (2010).
18. Urano, E. *et al.* Substitution of the myristoylation signal of human immunodeficiency virus type 1 Pr55Gag with the phospholipase C-delta1 pleckstrin homology domain results in infectious pseudovirion production. *J Gen Virol.* **89**, 3144–9 (2008).
19. Shimizu, S. *et al.* Inhibiting lentiviral replication by HEXIM1, a cellular negative regulator of the CDK9/cyclin T complex. *Aids.* **21**, 575–82 (2007).

Acknowledgments

This work was supported by the Japan Health Science Foundation, the Japanese Ministry of Health, Labor, and Welfare (H18-AIDS-W-003 to JK), and the Japanese Ministry of Education, Culture, Sports, Science and Technology (18689014 and 18659136 to JK).

Author contributions

K.M., E.U., M.T., R.I., and J.K. designed and performed experiments and interpret the data. J.K. wrote the manuscript. K.M. and E.U. equally contributed to this work.

Additional information

Competing financial interests: All authors declare no potential competing financial interests.

How to cite this article: Miyauchi, K., Urano, E., Takizawa, M., Ichikawa, R. & Komano, J. Therapeutic potential of HIV protease-activable CASP3. *Sci. Rep.* **2**, 359; DOI:10.1038/srep00359 (2012).

Structural Modulation Study of Inhibitory Compounds for Ribonuclease H Activity of Human Immunodeficiency Virus Type 1 Reverse Transcriptase

Hiroshi Yanagita,[a] Satoshi Fudo,[a] Emiko Urano,[b] Reiko Ichikawa,[b] Masakazu Ogata,[a] Mizuho Yokota,[a] Tsutomu Murakami,[b] Honggui Wu,[b,c] Joe Chiba,[c] Jun Komano,[b] and Tyuji Hoshino*[,a]

[a] *Graduate School of Pharmaceutical Sciences, Chiba University; 1–8–1 Inohana, Chuo-ku, Chiba 260–8675, Japan:* [b] *AIDS Research Center, National Institute of Infectious Diseases; 1–23–1 Toyama, Shinjuku-ku, Tokyo 162–8640, Japan: and* [c] *Faculty of Industrial Science and Technology, Tokyo University of Science; 2641 Yamazaki, Noda, Chiba 278–8510, Japan.* Received February 23, 2012; accepted April 4, 2012

Reverse transcriptase of human immunodeficiency virus type 1 (HIV-1) has two enzymatic functions. One of the functions is ribonuclease (RNase) H activity concerning the digestion of only RNA of RNA/DNA hybrid. The RNase H activity is an attractive target for a new class of anti-HIV drugs because no approved inhibitor is available now. In our previous studies, an agent bearing 5-nitro-furan-2-carboxylic acid ester core was found from chemical screening and dozens of the derivatives were synthesized to improve compound potency. In this work, some parts of the chemical structure were modulated to deepen our understanding of the structure–activity relationship of the analogous compounds. Several derivatives having nitro-furan-phenyl-ester skeleton were shown to be potent RNase H inhibitors. Attaching methoxy-carbonyl and methoxy groups to the phenyl ring increased the inhibitory potency. No significant cytotoxicity was observed for these active derivatives. In contrast, the derivatives having nitro-furan-benzyl-ester skeleton showed modest inhibitory activities regardless of attaching diverse kinds of functional groups to the benzyl ring. Both the modulation of the 5-nitro-furan-2-carboxylic moiety and the conversion of the ester linkage resulted in a drastic decrease in inhibitory potency. These findings are informative for designing potent inhibitors of RNase H enzymatic activity of HIV-1.

Key words antiviral drug; ribonuclease H enzymatic activity; nitro-furan-phenyl-ester; human immunodeficiency virus type 1 reverse transcriptase; inhibitor

Human immunodeficiency virus type 1 (HIV-1) reverse transcriptase (RT) is a multi-functional enzyme that facilitates both polymerase and ribonuclease (RNase) H activities and converts the single-stranded viral RNA into a double-stranded DNA. There exist two active sites in HIV-1 RT responsible for the respective enzymatic functions. Currently, two classes of RT inhibitors, nucleoside reverse transcriptase inhibitors (NRTIs) and non-nucleoside reverse transcriptase inhibitors (NNRTIs), are used clinically. The formers compete with the natural deoxyribonucleotide triphosphate (dNTP) for nucleoside incorporation and act as chain terminators after incorporation.[1] The latter agents are bound to an adjacent location from the polymerase active site and block RT polymerase function.[2] Both of these inhibitors are targeting polymerase activity of RT. In contrast, no approved inhibitor is available for RNase H activity, although there have been several reports on the inhibitors that target the RNase H activity of HIV-1 RT.[3–5] The role of RNase H activity in the reverse transcription process is to remove the viral genomic RNA during the synthesis of double-stranded DNA.[6,7] Agents targeting RNase H function is expected to be complimentary to the currently standard chemotherapy. Hence, RT-associated RNase H activity is one of the attractive targets for developing a novel class of antiviral drugs. Furthermore, the potential for dual inhibition of RNase H activity and integrase activity of HIV-1 has been examined because of the structural similarity of their catalytic sites.[8–10]

HIV-1 RNase H is known to utilize two divalent metals for catalysis.[11–13] The RNase H dual metal mechanism was suggested from high resolution co-crystal structures of *Bacillus halodurans* RNase H with RNA/DNA hybrids at different stages along the reaction pathway of phosphodiester cleavage.[14,15] The active site contains four carboxyl residues, creating an environment capable of holding two metal ions. It has been assumed that many RNase H inhibitors bind to the catalytic center interacting with two divalent metal ions simultaneously.

Diketo acids are known to work as potent inhibitors for divalent metal-related enzymes.[16] Therefore, diketo acid structure has served as a starting point for the design and optimization of inhibitors of HIV-1 integrase or influenza endonuclease. Pyrimidinol is another typical agent bearing a scaffold called *N*-hydroxyimide.[17] *N*-Hydroxyimides were firstly described as inhibitors of influenza endonuclease, but they also show a high potency in biochemical assays of HIV-1 RNase H. A natural product β-thujaplicinol is another scaffold and shows a high inhibitory potency for HIV-1 RNase H activity.[18]

From an *in vitro* screening using 20000 chemical compounds, we found chemicals that blocked HIV-1 RT-associated RNase H activity.[19] The agents bearing the 5-nitro-furan-2-carboxylic acid ester moiety turned out to work as an RNase H inhibitor. Two of the agents were capable of suppressing HIV-1 replication in tissue culture. On the basis of the hit chemicals found in the screening, more than 50 derivatives of 5-nitro-furan-2-carboxylic acid were synthesized.[20] Inhibitory potency of RNase H enzymatic activity was measured in a biochemical assay. Several derivatives showed higher

The authors declare no conflict of interest.

* To whom correspondence should be addressed. e-mail: hoshino@chiba-u.jp

inhibitory activities than those of the hit chemicals. Modulation of the 5-nitro-furan-2-carboxylic moiety resulted in a decrease in inhibitory potency. In contrast, many derivatives with modulation of other parts maintained inhibitory activities. These studies indicate that the nitro-furan-carboxylic moiety is one of the potent scaffolds for RNase H inhibitor.

In this study, we further synthesized chemical compounds bearing the 5-nitro-furan-2-carboxylic acid ester moiety and examined the potency for anti-HIV drugs blocking RT-associated RNase H enzymatic activity. The potency of the synthesized compounds was evaluated through the measurement of inhibitory activity with real-time monitoring of fluorescence emission from the digested RNA substrate. In addition, the cytotoxicity of these compounds was assessed in 293T cells. Computer simulation with molecular dynamics (MD) method was also performed to analyze the stability of the binding structure of an active compound.

Experimental

Organic Synthesis Compound **1** was synthesized by creating an ester linkage between a nitro-furan carboxylic acid and an α-chloro-amide bound with benzyl and penthyl groups, by 3 h reaction at 60°C in dimethylformamide (DMF) in the presence of dimethyl-aminopyridine (DMAP). Chemical modulation was performed for the nitro-furan moiety, with changing the starting block from furan to thiophene or pyrrole *etc.* **2–8**. These compounds **2–8** were synthesized in the similar manner to compound **1**. The derivatives bearing 5-nitro-furan-2-ester scaffold, compounds **9–27**, were prepared by the reaction of converting 5-nitro-2-furoic acid into an acid chloride with thionyl chloride, followed by the nucleophilic substitution reaction in the presence of NEt_3 in tetrahydrofuran (THF) with setting the temperature at 0°C for the initial 30 min. and elevated it to r.t. afterward. Since a hydroxy group bound to phenyl ring is more reactive than a hydroxy group bound to alkane, the substitution reaction dominantly produced phenyl-ester linkage (**9–16**) when a nucleophilic reagent contained two hydroxy groups. When a nucleophilic reagent contained only one hydroxy group, the substitution reaction generated alkyl-ester linkage (**17–27**). Compounds **28–30** were produced by generating nitro-furan-carbonyl-alkyl-benzene through the reaction of Weinreb amides containing benzyl group with alkyl lithium, followed by incorporation of nitro group into the phenyl ring using white fuming nitric acid and acetic anhydride. Compounds **29** and **30** were separated by flash chromatography. Compounds **31–33** were generated by using hydroxy-amines as nucleophilic reagents.

Evaluation of Inhibitory Activity The 50% inhibitory concentration (IC_{50}) of the synthesized compounds for RT-associated RNase H activity was determined from the chemical concentration reducing the rate for substrate cleavage reaction to half relative to the control. A real-time monitoring assay was employed to estimate the IC_{50}.[21,22] In short, two oligo-nucleotides were annealed at final concentrations of 2.5 and 0.25 μM for substrate. One was oligo-ribonucleotide 5′-GAUCUGAGCCUGGGAGCU-3′ with 6-carboxy-fluoroscein (FAM) conjugated at the 3′ end, and the other was oligo-deoxyribonucleotide 5′-AGCTCCCAGGCTCAGATC-3′ with black hole quencher (BHQ) conjugated at the 5′ end. Enzyme reaction with 100 ng RT, 0.025 μM oligo-ribonucleotide, and 0.25 μM oligo-deoxyribonucleotide was carried out in a volume of 10 μL at 37°C. Fluorescence at 488 nm was monitored every 150 s using a multimode detector.

HIV-1 RT was expressed in *Escherichia coli* and purified by using a HiTrap Ni affinity column. The purified RT was dialyzed to reduce the concentration of imidazole from the elution buffer and then incubated with human rino virus (HRV) 3C protease to cleave an N-terminal hexahistidine tag. The protein was further purified by nickel-coordinated nitrilotriacetic acid (Ni-NTA) to remove the uncleaved protein and HRV 3C protease. The RT was dialyzed against a buffer of 50 mM Tris–HCl at pH 7.5 and 200 mM NaCl and was stored at −20°C with adding 50% (v/v) glycerol.

Assessment of Cytotoxicity 3-(4,5-Dimethylthiazol-2-yl)-2,5-diphenyltetrazolium bromide (MTT) assay was carried out with 293T cell line. First, 100 μL medium (RPMI-1640) supplemented with 10% fetal bovine serum (FBS) containing 2% dimethylsulfoxide (DMSO) was loaded in a 96-well plate, and 200 μL medium with 10% FBS and 2% DMSO containing test compounds at a concentration of 200 μM was added to the wells in the first column of the plate. Different concentrations of compound were prepared for the second, third and fourth columns. The final concentrations of these columns were 100, 50, 25 and 12.5 μM, respectively. Second, 100 μL 293T cells at a concentration of 2×10^5/mL were added to the respective wells. The final concentration of DMSO in each well was 1%. Third, cells were incubated for 3 d at 37°C with 5% CO_2 atmosphere. A hundred micro liter of supernatant was removed from the cultured medium and 15 μL MTT reagent for dye solution was added to each well and the cells were incubated for 1 h. Then, 100 μL solution of stop mix was added, and the cells were incubated overnight at 4°C to sufficiently dissolve the dye. Finally, intensity of $OD_{570/690}$ was measured by a spectrofluorometer.

Molecular Dynamics Simulation A computational model of HIV-1 RT domain was constructed from an X-ray crystal structure with Protein Data Bank code 3QIO.[23] Atom coordinates for the missing residues were generated by using Modeller9.9.[24] According to the results of the recent X-ray crystallographic studies on the complex of RNase H domain and its inhibitors,[25–27] the RNase H domain contains two divalent metal ions at the center of the active site. Two Mn^{2+} ions in the crystal structure were replaced with Mg^{2+} ions. The protonation states of all of the ionazable residues were predicted by ProPKa program[28] in the presence of two Mg^{2+} ions at the active site. Atom charges of the compounds were determined from the electrostatic potential obtained from quantum chemical calculations, followed by the restrained electrostatic potential (RESP) fitting[29] in a similar manner to the previous studies.[30–33] The atom charge for Mg^{2+} ion was setting to 1.54, which was also determined by the RESP method based on the calculated electrostatic potential obtained by QM/MM technique carried out in a similar manner to the previous work.[20] An active compound was combined with HIV-1 RT domain, referring the binding structure predicted in our previous work.[20] The compound-bound RT model was placed in a rectangular box and solvated with TIP3P water molecules,[34] with all of the crystal water molecules remaining. Periodic boundary conditions were applied to avoid the edge effect in all calculations.

Minimizations and MD simulations were carried out using sander module of AMBER9.[35] The modified ff03 force field[36]

was used as the parameters for molecular dynamics. The cut-off distance for the long range electrostatic and van der Waals energy terms was set to 12.0 Å. The expansion and shrinkage of all covalent bonds connecting to hydrogen atom were constrained using the SHAKE algorithm.[37] Energy minimization was achieved in three steps. Initially, movement was allowed only for water molecules. Next, compound and divalent metal ions were allowed to move in addition to the water molecules. Finally, all atoms were allowed to move freely. In each step, energy minimization was executed by the steepest descent method for the first 10000 cycles and the conjugated gradient method for the subsequent 10000 cycles. After a 0.1 ns heating calculation until 310 K using the NVT ensemble condition, a 20 ns equilibrating calculation was executed at 1.0 atm and at 310 K under the NPT ensemble condition, with an integration time step of 2.0 fs.

Results

Eight analogues of 5-nitro-furan-2-carboxylic acid ester were synthesized by converting the 5-nitro-furan moiety into other functional groups and examined for their RNase H inhibitory activities (Table 1). Compound **1** has a typical chemical structure showing an inhibitory potency for HIV-1 RNase H enzymatic activity. This compound bears nitro-furan ester core connecting to the pentyl- and benzyl-bound amide group. Replacement of furan with thiophene largely decreased compound potency (**2**, **3**). Conversion of furan into pyrrole also resulted in complete loss of compound potency (**4**). Attaching a halogen to the 4th position of furan exhibited a slight increase of inhibitory activity (**5**), while a hydrophobic or aromatic substitute resulted in loss of inhibitory potency (**6**, **7**). Introduction of even a small hydrophobic group at the 3rd position of furan decreased inhibitory activity (**8**).

Table 1. RNase H Inhibitory Activity and Cytotoxicity of the Derivatives Modulated at Nitro-Furan Moiety

Compound	Structure	IC_{50} (μM)	CC_{50} (μM)
1	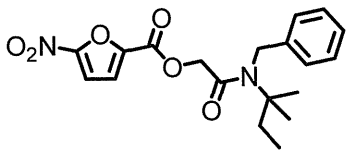	8.4	74
2	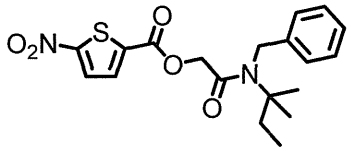	>50	49
3	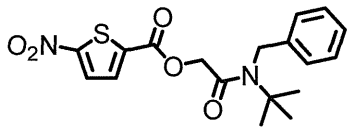	30.3	50
4	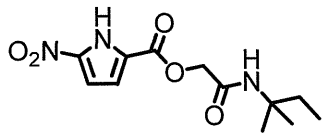	>50	86
5	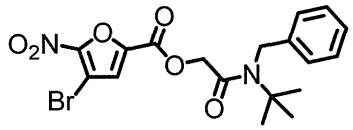	6.6	3
6	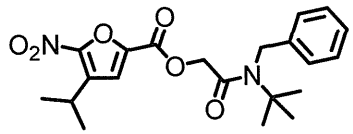	>50	>100
7	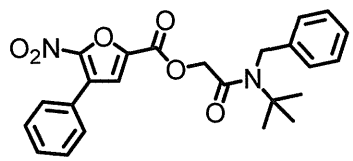	>50	>100
8	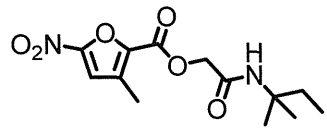	25.7	76

Eight derivatives bearing 5-nitro-furan phenyl ester core were examined as shown in Table 2. A similar degree of inhibitory activity was observed for the analogs having a hydroxy group at the *meta* or *para* position of phenyl ring (**9**–**11**). While substitution of the hydroxy group with acetyl group showed a similar degree of inhibitory activity (**12**), substitution with ethyl-ester increased compound potency (**13**). Further, introduction of methoxy group at the *ortho* position also increased compound potency (**14**). The compound containing methoxy-carbonyl and methoxy groups at the *para* or *ortho* positions exhibited a fine inhibitory activity (**15**). Introduction of phenyl-methyl-amine at the *para* position also maintained compound potency (**16**).

Eleven derivatives bearing 5-nitro-furan ester core bound with benzyl-based substitutes were investigated as summarized in Table 3. Connection of a benzyl group without any additional functional substitute showed moderate inhibitory activity (**17**). Attaching nitro group, methoxy-ether, or *tert*-butoxy-ester exhibited slight changes in compound potency (**18**–**20**). Extension of alkyl chain caused no significant difference in inhibitory potency (**21**). However, addition of hydroxy group decreased inhibitory activity (**22**). Introduction of methoxy group further decreased compound potency regardless of the position of the group bound to phenyl ring (**23**–**25**). While connection of two methoxy groups improved compound potency (**26**), replacement of two methoxy groups by chlorides showed low inhibitory activity (**27**).

Six derivatives were synthesized by changing the ester bond with carbonyl group as shown in Table 4. Ester linkage is disadvantageous for medicine because esterase digests the linkage and the drug concentration in a body decreases rapidly. Nitro-phenyl group was connected to the carbonyl carbon with changing the length of alkyl chain and the position of nitro group (**28**–**30**). None of the derivatives showed noticeable inhibitory activity. The ester linkage was replaced by an amide bond (**31**–**33**), in which hydroxy-methyl-benzyl, acetyl-methyl-benzyl, or bromo-methyl-benzyl was bound *via* a carbamoyl group. This modification also resulted in complete loss of compound potency.

Table 2. RNase H Inhibitory Activity and Cytotoxicity of the Derivatives Bearing Phenyl Ester Core

Compound	–O–R	IC_{50} (μM)	CC_{50} (μM)
9	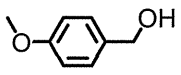	7.2	>100
10	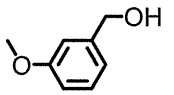	8.2	24
11	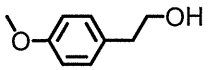	9.1	>100
12	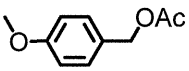	8.7	49
13	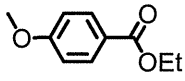	3.6	>100
14	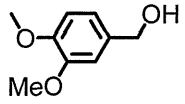	3.1	>100
15	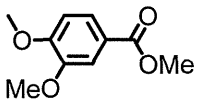	1.4	>100
16	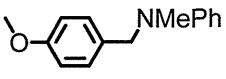	3.8	>100

Cytotoxicity was little or undetectable for most of the derivatives modulated at the nitro-furan moiety except for compound **5** (Table 1). No detectable cytotoxicity was also observed for most of the derivatives bearing nitro-furan-phenyl ester core (Table 2). It should be noted that highly active compounds, **14** and **15**, showed no noticeable cytotoxicity at a concentration of 100 μM. In contrast, the analogs bearing ester core bound with benzyl-based substitute showed some degree of cytotoxicity (Table 3). Further, the analogs converted the ester into amide or ketone showed cytotoxicity in which CC_{50} ranged from 9 to 32 μM (Table 4). Overall, in the measurement using 293T cells, half of the synthesized compounds showed noticeable cytotoxicity but almost all of the toxicity-detected compounds showed little RNase H inhibitory activity. Accordingly, the results of this assay suggest that active compounds have no significant cytotoxicity and the nitro-furan-phenyl ester skeleton is the most favorable among them from a cytotoxic viewpoint.

In order to examine the stability of the binding structure of a potent compound inside the active site of the target protein, MD simulation was performed for the complex of a synthesized derivative **15** and RNase H domain. MD simulation was carried out for 20 ns and root mean square deviation (RMSD) relative to the structure after heating was calculated as shown in Fig. S1 of the supplemental information. The RMSD value showed a gradual increase up to 5 ns and scarcely changed during later 15 ns. Accordingly, the binding conformation of the complex was judged to be equilibrated. In order to extract the snapshot structure representing a typical binding mode of compound **15** and RNase H domain, the averaged structure was obtained using 2500 trajectories from the last 5 ns of MD simulation. The RMSD between each trajectory and the average structure was calculated, and then one trajectory with the smallest RMSD value was determined to be the typical complex structure shown in Fig. 1a.

Two Mg^{2+} ions were held by the side chains of four acid residues; Asp443, Glu478, Asp498, Asp549, and the compound was stably bound to the active site without changing the binding mode during 20 ns simulation. In the binding structure, the nitro-furan-ester core is especially, stably bound to two Mg^{2+} ions as shown in Fig. 1a. A stereo view of the binding structure is presented in Fig. S2 of the supplemental information. The oxygen atom on the furan ring is oriented toward the divalent metals. Nitro oxygen and carbonyl oxygen of the ester are strongly coordinated to the respective Mg^{2+} ions. Therefore, a large ring-shaped configuration of –Mg–O–N–C–O–C–C–O–Mg– is formed. The inter-atomic distance between two Mg^{2+} ions is 3.8 Å. The distance between the nitro oxygen atom and one Mg^{2+} ion is 1.9 Å, and that between carbonyl oxygen and the other Mg^{2+} ion is also 1.9 Å. Figure

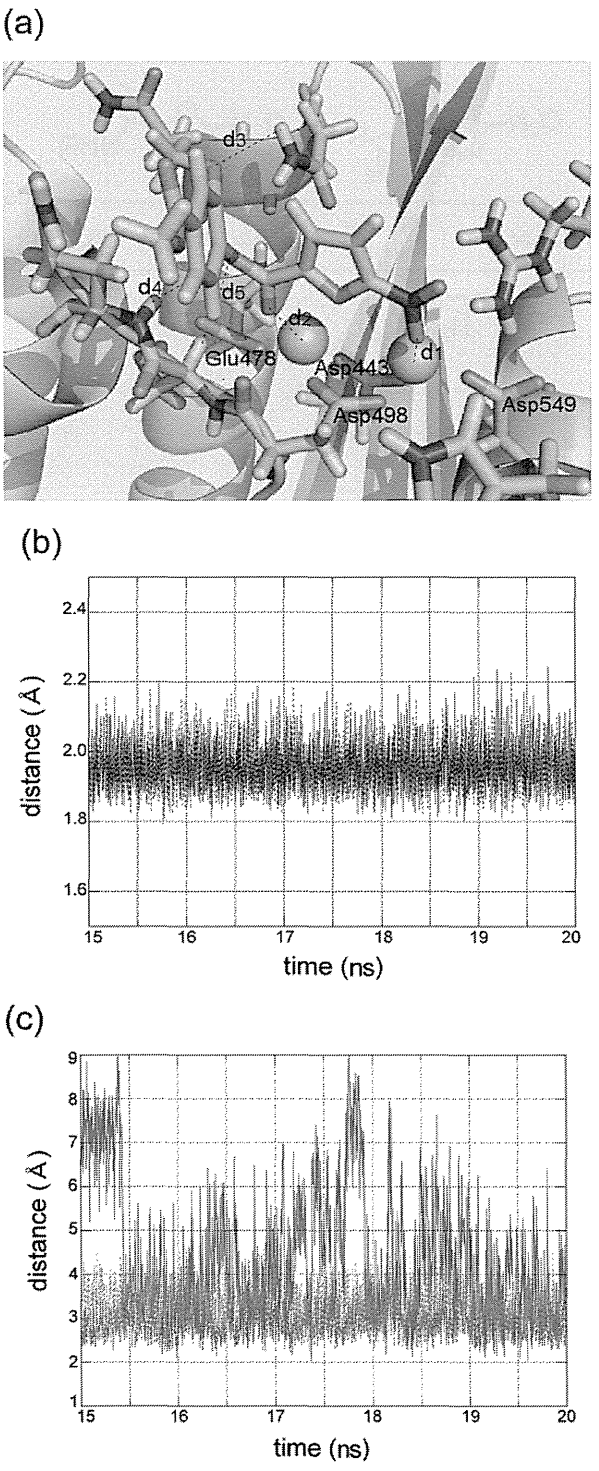

Fig. 1. (a) Binding Structure of an Active Compound to the RNase H Domain, Obtained by MD Simulation

Compound and several polar residues are shown in stick representation. Two Mg^{2+} ions are denoted by spheres. (b) Changes in the distances between nitro oxygen and Mg^{2+} ion (d_1: red solid line) and between carbonyl oxygen and another Mg^{2+} ion (d_2: blue dotted line) for the last 5 ns of MD simulation. (c) Changes in the distances between methoxy oxygen and amino hydrogen of Asn474 (d_3: green solid line), between ester oxygen and amide hydrogen of main chain of Gln500 (d_4: cyan broken line), and between ester oxygen and Cα hydrogen of Ser499 (d_5: yellow dotted line) for the last 5 ns of MD simulation. Color images were converted into gray scale; red solid line, blue dotted line, green solid line, cyan broken line, yellow dotted line have been converted into gray scale.

1b shows the changes of these two distances for the last 5 ns of MD simulation. These graphs clearly indicate that the interaction of oxygen atom and Mg^{2+} ion is quite strong and that the oxygen–Mg interaction is essentially important for the binding of potent compound.

Methoxy-carbonyl and methoxy groups connected to phenyl stick out from the binding pocket. The distance between methoxy oxygen and hydrogen atom of amino group of Asn474 was monitored as shown in Fig. 1c. The distance largely fluctuates during the simulation and the interaction is not so steady. Hence, there is much room for improvement in this region. The oxygen atom at the ester bond has noticeable interactions with the amide group of main chain of Gln500. The change of the distance between the ester oxygen and the hydrogen atom of the amide group is shown in Fig. 1c. No abrupt, large change is observed in the distance. Therefore, the interaction contributes to stabilizing the binding of the potent compound. The distance between the ester oxygen and the Cα hydrogen atom of Ser 499 was also monitored. The distance shows no large change for the last 5 ns of simulation, which suggests the stability of the binding of the ester part with RNase H domain. Consequently, it is confirmed from the MD simulation that an active compound **15** is stably bound to the active site of the RNase H domain with coordinating to two divalent metal ions and making supportive interaction at the ester part.

Discussion

According to the data summarized in Table 3, it is suggested that various kinds of functional groups connected to the benzyl ring have little interaction with the RNase H domain and that the functional group-binding region is located outside the binding pocket and is exposed to the solvent. Further, a comparison of inhibitory activity between compounds **17**–**20** and compounds **21**–**27** suggests that the length of alkyl chain connecting to phenyl ring has a significant influence on the difference in compound potency. That is, the longer alkyl chain in compounds **21**–**27** is less favorable in terms of both inhibitory activity and cytotoxicity. This indicates that a strategy to increase the inhibitory activity is to position the substitute closer to the nitro-furan group. The conversion may allow the aromatic ring or substitute to interact with the target protein inside the binding pocket.

A comparison of inhibitory activities of compounds in Tables 2 and 3 indicates that the introduction of phenyl-ester connected to nitro-furan shows higher compound potency than that of benzyl-ester. This is consistent with the findings described above paragraph and supports the notion that the compound potency increases when the position of the substitute connected to the ester linkage is closer to the nitro-furan. The incorporation of polarized substitutes like methoxy, hydroxy, methoxy-carbonyl, or ethoxy-carbonyl group is effective to increase the compound potency. In particular, the introduction of methoxy group at the *ortho*-position of phenyl ring effectively increases the inhibitory activity.

All the compounds in Tables 2 and 3 have the ester linkage. The data summarized in Table 4 clearly indicate that conversion of the ester linkage into carbonyl and/or amide bond results in loss of inhibitory potency. Both bonds will be likely to make the chemical to be in a straight configuration. If a compound has a straight form, the side part of the compound

Table 3. RNase H Inhibitory Activity and Cytotoxicity of the Derivatives Bearing Ester Core Bound with Benzyl-Based Substitute

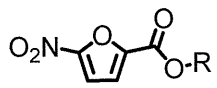

Compound	–O–R	IC_{50} (μM)	CC_{50} (μM)
17	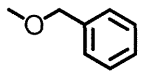	5.4	38
18	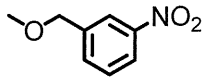	5.0	>100
19	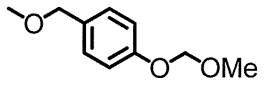	5.8	75
20	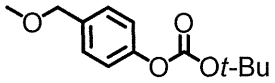	4.5	>100
21	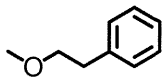	5.1	57
22	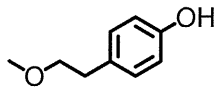	7.9	39
23	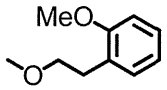	14.2	42
24	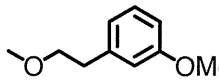	18.6	36
25	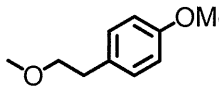	12.5	36
26	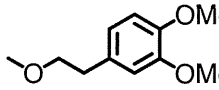	8.5	51
27	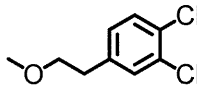	17.4	64

Table 4. RNase H Inhibitory Activity and Cytotoxicity of the Derivatives Converted the Ester Bond into Other Kinds of Linkages

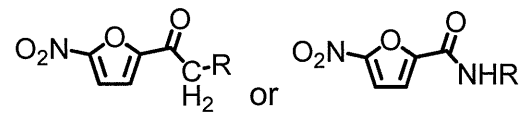

Compound	$-CH_2-R$ or –NH–R	IC_{50} (μM)	CC_{50} (μM)
28	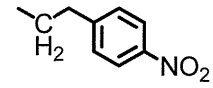	>50	11
29	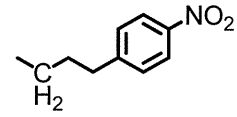	>50	17
30	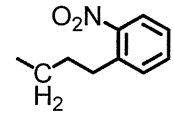	>50	9
31	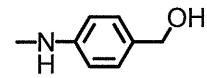	>50	29
32	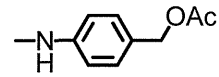	>50	27
33	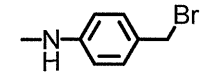	>50	32

will collide with the inside wall of the binding pocket of the RNase H domain. Accordingly, compounds are hardly combined with the binding pocket.

The conversion of the nitro-furan group into pyrrole drastically decreases the inhibitory activity while conversion to nitro-thiophen maintains the activity (Table 1). This indicates that a nitro-furan or nitro-thiophene core is indispensable for inhibitory potency. The characteristic property of nitro-furan is its large electric polarity. Oxygen atoms are negatively charged and these oxygen atoms will be coordinated to divalent metal ions at the RNase H active site. The attachment of non-polar substitute to furan results in decrease of compound potency. Accordingly, the 3rd and 4th positions of furan become close to the residues inside the RNase H active site.

RNase H of HIV-1 exerts its enzymatic activity by incorporating divalent metal ions at the reaction site.[38,39] It had been controversial how many metal ions were required at the RNase H reaction site to exert its enzymatic activity.[40] A theoretical study by De Vivo *et al.* suggested that the presence of two divalent metal ions is essential for RNase H activity and that two metal ions act cooperatively with facilitating the binding of a substrate and catalyzing the enzymatic reaction.[41] This theoretical finding strongly suggests double coordination of divalent metal ions at the RNase H domain. Crystal structures on the complex of the RNase H domain and its inhibitor were successively reported from three different research groups.[23,25–27] All of the crystal structures ever reported showed the presence of two metal ions at the active site. One of the divalent metal ions was held deep inside the binding pocket of the RT RNase H domain with making coordination bonds to three carboxyl groups of Asp443, Glu478 and Asp498. The other was fixed with making coordination bonds to two carboxyl groups of Asp443 and Asp549. The distance between two metal ions was about 4 Å. Every inhibitor in crystal structures was revealed to have a similar binding mode. That is, inhibitors are stabilized with forming coordination bonds to both metal ions. Accordingly, it is highly probable that the chemical compounds showing RNase H inhibitory activity examined in this study are also coordinated to two divalent metal ions. Hence, negatively charged oxygen atoms of the nitro group, furan, and carbonyl group are aligned in a straight form. This negatively charged region will be attached to the divalent metal ions.

The binding structure deduced from MD simulation indicates that ether oxygen at the ester bond has an interaction with a polar residue, Ser499, which is located at the deep inside of RNase H domain. This residue would have little

influence on the function of RNase H. Therefore, one of the designs to improve inhibitory activity is to modify the compound to bear some polar functional group that enables a strong interaction with Ser499. In order to enhance the binding affinity of the compounds with RNase H active site, the incorporation of a polar functional group bound to phenyl ring is one of the possible conversions of our derivatives. The distance between methoxy group and the amine of Asn474 largely fluctuated during MD simulation. If the interaction with Asn474 is enforced, compound will be more stably combined with the RNase H domain.

Conclusion

More than 30 chemical compounds were synthesized for developing the inhibitors of RNase H activity of HIV-1 reverse transcriptase. Inhibitory potency of RNase H enzymatic activity was measured in a biochemical assay with a real-time fluorescence monitoring method. The active compounds found in our previous studies commonly bear nitro-furan ring connecting to hydrophobic region *via* an ester linkage. Conversion of the nitro-furan group into pyrrole drastically decreased the inhibitory activity while conversion into nitro-thiophene maintained the compound potency. This means that the structural basis of nitro-furan or nitro-thiophene is indispensable for inhibitory activity. An improvement in compound potency was observed when a phenyl-ester moiety was connected to the nitro-furan and further methoxy-carbonyl and methoxy groups were bound to the phenyl ring. No notable change in inhibitory potency was observed when benzyl-ester based substitute was connected to nitro-furan. Modulation of ester linkage resulted in complete loss of compound potency. Molecular dynamics simulation was performed to examine the stability of the binding structure of a synthesized active compound to RNase H domain. It was demonstrated that a potent compound was stably bound to the active site with establishing strong coordinate bonds with divalent metal ions located at the active site. The present study provides important information for designing prospective chemical structures inhibiting HIV-1 RNase H activity.

Acknowledgments This work was supported by a Health and Labor Science Research Grant for Research on Publicly Essential Drugs and Medical Devices from the Ministry of Health and Labor of Japan. A part of this work was also supported by a Grant-in-Aid for Scientific Research (C) from Japan Society for the Promotion of Science (JSPS). Theoretical calculations were performed at the Research Center for Computational Science, Okazaki, Japan and at the Information Technology Center of the University of Tokyo and also by the high-performance computer system at Institute for Media Information Technology in Chiba University.

References

1) Goody R. S., Müller B., Restle T., *FEBS Lett.*, **291**, 1–5 (1991).
2) Ren J., Stammers D. K., *Virus Res.*, **134**, 157–170 (2008).
3) Andréola M. L., De Soultrait V. R., Fournier M., Parissi V., Desjobert C., Litvak S., *Expert Opin. Ther. Targets*, **6**, 433–446 (2002).
4) Klumpp K., Mirzadegan T., *Curr. Pharm. Des.*, **12**, 1909–1922 (2006).
5) Tramontano E., *Mini Rev. Med. Chem.*, **6**, 727–737 (2006).
6) Tanese N., Telesnitsky A., Goff S. P., *J. Virol.*, **65**, 4387–4397 (1991).
7) Telesnitsky A., Goff S. P., *EMBO J.*, **12**, 4433–4438 (1993).
8) Borkow G., Fletcher R. S., Barnard J., Arion D., Motakis D., Dmitrienko G. I., Parniak M. A., *Biochemistry*, **36**, 3179–3185 (1997).
9) Tramontano E., Esposito F., Badas R., Di Santo R., Costi R., La Colla P., *Antiviral Res.*, **65**, 117–124 (2005).
10) Tarrago-Litvak L., Andreola M. L., Fournier M., Nevinsky G. A., Parissi V., de Soultrait V. R., Litvak S., *Curr. Pharm. Des.*, **8**, 595–614 (2002).
11) Cowan J. A., Ohyama T., Howard K., Rausch J. W., Cowan S. M., Le Grice S. F., *J. Biol. Inorg. Chem.*, **5**, 67–74 (2000).
12) Haren L., Ton-Hoang B., Chandler M., *Annu. Rev. Microbiol.*, **53**, 245–281 (1999).
13) Steitz T. A., Smerdon S. J., Jäger J., Joyce C. M., *Science*, **266**, 2022–2025 (1994).
14) Nowotny M., Gaidamakov S. A., Crouch R. J., Yang W., *Cell*, **121**, 1005–1016 (2005).
15) Nowotny M., Gaidamakov S. A., Crouch R. J., Yang W., *EMBO J.*, **25**, 1924–1933 (2006).
16) Shaw-Reid C. A., Munshi V., Graham P., Wolfe A., Witmer M., Danzeisen R., Olsen D. B., Carroll S. S., Embrey M., Wai J. S., Miller M. D., Cole J. L., Hazuda D. J., *J. Biochem.*, **278**, 2777–2780 (2003).
17) Hang J. Q., Rajendran S., Yang Y., Li Y., In P. W. K., Overton H., Parkes K. E. B., Cammack N., Martin J. A., Klumpp K., *Biochem. Biophys. Res. Commun.*, **317**, 321–329 (2004).
18) Budihas S. R., Gorshkova I., Gaidamakov S., Wamiru A., Bona M. K., Parniak M. A., Crouch R. J., McMahon J. B., Beutler J. A., Le Grice S. F., *Nucleic Acids Res.*, **33**, 1249–1256 (2005).
19) Fuji H., Urano E., Futahashi Y., Hamatake M., Tatsumi J., Hoshino T., Morikawa Y., Yamamoto N., Komano J., *J. Med. Chem.*, **52**, 1380–1387 (2009).
20) Yanagita H., Urano E., Matsumoto K., Ichikawa R., Takaesu Y., Ogata M., Murakami T., Wu H. G., Chiba J., Komano J., Hoshino T., *Bioorg. Med. Chem.*, **19**, 816–825 (2011).
21) Chan K. C., Budihas S. R., Le Grice S. F., Parniak M. A., Crouch R. J., Gaidamakov S. A., Isaaq H. J., Wamiru A., McMahon J. B., Beutler J. A., *Anal. Biochem.*, **331**, 296–302 (2004).
22) Parniak M. A., Min K. L., Budihas S. R., Le Grice S. F., Beutler J. A., *Anal. Biochem.*, **322**, 33–39 (2003).
23) Lansdon E. B., Liu Q., Leavitt S. A., Balakrishnan M., Perry J. K., Lancaster-Moyer C., Kutty N., Liu X., Squires N. H., Watkins W. J., Kirschberg T. A., *Antimicrob. Agents Chemother.*, **55**, 2905–2915 (2011).
24) Martí-Renom M. A., Stuart A. C., Fiser A., Sánchez R., Melo F., Sali A., *Annu. Rev. Biophys. Biomol. Struct.*, **29**, 291–325 (2000).
25) Kirschberg T. A., Balakrishnan M., Squires N. H., Barnes T., Brendza K. M., Chen X., Eisenberg E. J., Jin W., Kutty N., Leavitt S., Liclican A., Liu Q., Liu X., Mak J., Perry J. K., Wang M., Watkins W. J., Lansdon E. B., *J. Med. Chem.*, **52**, 5781–5784 (2009).
26) Himmel D. M., Maegley K. A., Pauly T. A., Bauman J. D., Das K., Dharia C., Clark A. D. Jr., Ryan K., Hickey M. J., Love R. A., Hughes S. H., Bergqvist S., Arnold E., *Structure*, **17**, 1625–1635 (2009).
27) Su H. P., Yan Y., Prasad G. S., Smith R. F., Daniels C. L., Abeywickrema P. D., Reid J. C., Loughran H. M., Kornienko M., Sharma S., Grobler J. A., Xu B., Sardana V., Allison T. J., Williams P. D., Darke P. L., Hazuda D. J., Munshi S., *J. Virol.*, **84**, 7625–7633 (2010).
28) Li H., Robertson A. D., Jensen J. H., *Proteins*, **61**, 704–721 (2005).
29) Cieplak P., Cornell W. D., Bayly C., Kollman P. A., *J. Comput. Chem.*, **16**, 1357–1377 (1995).
30) Matsuyama S., Aydan A., Ode H., Hata M., Sugiura W., Hoshino T., *J. Phys. Chem. B*, **114**, 521–530 (2010).
31) Sano E., Li W., Yuki H., Liu X., Furihata T., Kobayashi K., Chiba K., Neya S., Hoshino T., *J. Comput. Chem.*, **31**, 2746–2758 (2010).

2) Ode H., Neya S., Hata M., Sugiura W., Hoshino T., *J. Am. Chem. Soc.*, **128**, 7887–7895 (2006).
3) Ode H., Matsuyama S., Hata M., Neya S., Kakizawa J., Sugiura W., Hoshino T., *J. Mol. Biol.*, **370**, 598–607 (2007).
4) Jorgensen W. L., Chandrasekhar J., Madura J. D., Impey R. W., Klein M. L., *J. Chem. Phys.*, **79**, 926–935 (1983).
5) Case D. A., Darden T. A., Cheatham T. E. III, Simmerling C. L., Wang J., Duke R. E., Luo R., Merz K. M., Pearlman D. A., Crowley M., Walker R. C., Zhang W., Wang B., Hayik S., Roitberg A., Seabra G., Wong K. F., Paesani F., Wu X., Brozell S., Tsui V., Gohlke H., Yang L., Tan C., Mongan J., Hornak V., Cui G., Beroza P., Mathews D. H., Schafmeister C., Ross W. S., Kollman P. A., "AMBER 9," University of California, San Francisco, 2006.
6) Katagiri D., Fuji H., Neya S., Hoshino T., *J. Comput. Chem.*, **29**, 1930–1944 (2008).
37) Ryckaert J.-P., Ciccotti G., Berendsen H. J. C., *J. Comput. Phys.*, **23**, 327–341 (1977).
38) Sarafianos S. G., Das K., Tantillo C., Clark A. D. Jr., Ding J., Whitcomb J. M., Boyer P. L., Hughes S. H., Arnold E., *EMBO J.*, **20**, 1449–1461 (2001).
39) Huang H., Chopra R., Verdine G. L., Harrison S. C., *Science*, **282**, 1669–1675 (1998).
40) Klumpp K., Hang J. Q., Rajendran S., Yang Y., Derosier A., Wong Kai In P., Overton H., Parkes K. E., Cammack N., Martin J. A., *Nucleic Acids Res.*, **31**, 6852–6859 (2003).
41) De Vivo M., Dal Peraro M., Klein M. L., *J. Am. Chem. Soc.*, **130**, 10955–10962 (2008).

ACS chemical biology

Articles

pubs.acs.org/acschemicalbiology

Mechanism of Drug Resistance of Hemagglutinin of Influenza Virus and Potent Scaffolds Inhibiting Its Function

Hiroshi Yanagita,[†,#] Norio Yamamoto,[‡,§,#,*] Hideyoshi Fuji,[†] Xinli Liu,[†] Masakazu Ogata,[†] Mizuho Yokota,[†] Hiroshi Takaku,[∥] Hideki Hasegawa,[⊥] Takato Odagiri,[‡] Masato Tashiro,[‡] and Tyuji Hoshino[†,*]

[†]Graduate School of Pharmaceutical Sciences, Chiba University, Inohana 1-8-1, Chuo-ku, Chiba 260-8675, Japan

[‡]Influenza Virus Research Center and [⊥]Department of Pathology, National Institute of Infectious Diseases, 4-7-1 Gakuen, Musashimurayama, Tokyo 208-0011, Japan

[§]Department of General Medicine, Juntendo University School of Medicine, 2-1-1 Hongo, Bunkyo-ku, Tokyo 113-8421, Japan

[∥]Department of Life and Environmental Science, Chiba Institute of Technology, 2-17-1 Tsudanuma, Narashino-shi, Chiba 275-0016, Japan

Supporting Information

ABSTRACT: Highly pathogenic influenza viruses have become a global threat to humans. It is important to select an effective therapeutic option suitable for the subtypes in an epidemic or pandemic. To increase the options, the development of novel antiviral agents acting on targets different from those of the currently approved drugs is required. In this study, we performed molecular dynamics simulations on a spike protein on the viral envelop, hemagglutinin, for the wild-type and three kinds of mutants using a model system consisting of a trimeric hemagglutinin complex, viral lipid membrane, solvation waters, and ions. A natural product, stachyflin, which shows a high level of antiviral activity specific to some subtypes of influenza viruses, was examined on binding to the wild-type hemagglutinin by docking simulation. The compound potency of stachyflin is, however, easily lost due to resistant mutations. From a comparison of simulation results between the wild-type and the resistant mutants, the reason for the drug resistance of hemagglutinin was clarified. Next, 8 compounds were selected from a chemical database by *in silico* screening, considering the findings from the simulations. Inhibitory activities to suppress the proliferation of influenza virus were measured by cell-based antiviral assays, and two chemical scaffolds were found to be potent for an inhibitor. More than 30 derivatives bearing either of these two chemical scaffolds were synthesized, and cell culture assays were carried out to evaluate the compound potency. Several derivatives displayed a high compound potency, and 50% effective concentrations of two synthesized compounds were below 1 μM.

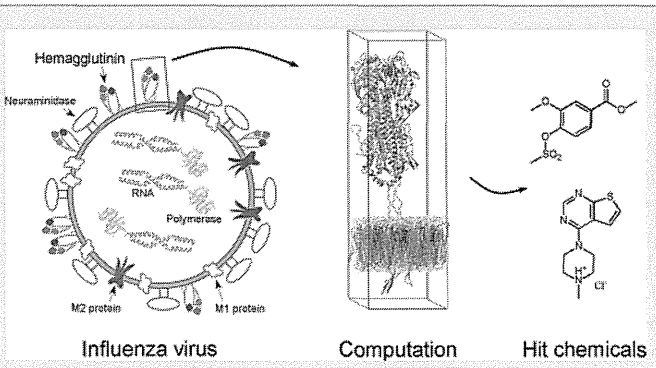

Influenza viruses cause acute respiratory infection in humans that occasionally progresses to a severe pulmonary condition. Even seasonal epidemics account for 300,000 or more deaths per a year all over the world. Recently, the emergence of highly pathogenic avian and swine influenza viruses has become a global threat to humans. Avian influenza H5N1 virus infections have been reported since 2003,[1] and a pandemic of transmissible H5N1 virus is a serious concern for public health.[2] The recent outbreak of swine influenza subtype H1N1 resulted in considerable mortalities for infants and the elderly. While several anti-influenza drugs are currently approved, their effectiveness for pandemic viruses may be limited due to drug resistance. Therefore, the development of additional antiviral agents against influenza virus infection is needed.

The currently available anti-influenza drugs target one of two viral proteins: M2 protein and neuraminidase. M2 protein is embedded in the lipid membrane of the viral envelope and functions as an ion channel to pump protons into the viral particles. Amantadine and Rimantadine block the function of M2 protein by combining at the center of the channel or the side domain of this enzyme.[3,4] Neuraminidase is a kind of spike protein sticking out on the viral particle surface. Neuraminidase causes the hydrolysis of neuraminic acid of the glycan of the host cell. Zanamivir, Oseltamivir, Peramivir, and Laninamivir have been used as neuraminidase inhibitors.[5,6] Emergence of drug-resistant viruses has been reported for the above approved

Received: September 1, 2011
Accepted: January 4, 2012
Published: January 4, 2012

drugs. For example, resistance against Amantadine and Rimantadine was shown in the H3N2 and H1N1 viruses, and resistance against Oseltamivir was shown for the H1N1 virus.[7−9] Since an RNA virus easily acquires amino acid mutations, the emergence rate of drug-resistant viruses is high. A drug-resistant virus is a serious issue in infectious diseases because a chemotherapeutic approach is restricted. In order to combat drug-resistant viruses, it is important to prepare many chemotherapeutic options and select an effective option suitable for subtypes in an epidemic. Accordingly, development of novel antiviral drugs that act on a target different from those of the currently approved drugs is needed.

A species of moss, Stachybotrys s. RF-7260, generates a unique natural product named stachyflin. Stachyflin was found to have strong antiviral activity against some subtypes of influenza viruses.[10−12] The inhibitory mechanism of stachyflin is different from the inhibitory mechanism of the currently approved anti-influenza drugs. Stachyflin binds with hemagglutinin (HA) on the viral envelope and blocks conformation change of HA to prevent the lipid membrane of the viral envelope from merging with that of host cell. HA is one of the attractive targets of antiviral agents for the following reasons. First, HA is a key component in the viral infusion process that has no cellular counterparts and therefore has a potential advantage in selectivity and toxicity. Second, HA inhibitors will complement other currently approved drugs since they act on a different molecular target in the virus life cycle.

Stachyflin is highly effective for influenza virus of A/WSN/33 H1N1 subtype, and the 50% inhibitory concentration (IC_{50}) value for the WSN strain was reported to be 3 nM.[12] However, its inhibitory activity for other strains including other H1N1 virus strains is not so high, and its inhibitory activity is easily decreased by amino acid mutations of the virus. Since several amino acid mutations involved in drug resistance are not localized in one domain of HA, it is difficult to understand the mechanism of drug resistance caused by mutations straightforwardly. The chemical structure of stachyflin is complicated. Five rings merge to form a structure called the 3*H*-naphtho-pyrano-isoindol-3-one scaffold, and stachyflin also contains five chiral centers (Figure 1a). This complexity in its chemical structure is another reason for the difficulty in improving compound potency for stachyflin derivatives.

Yoshimoto and co-workers performed an experiment on resistance induction with stachyflin[13] and demonstrated that K51R, K121E, S206L in the HA2 subunit and V176I in the HA1 subunit appeared in resistant viruses (Figure 1b). K51R and K121E mutations were suggested to be essential for drug resistance. They suggested from a docking simulation that stachyflin was bound to a position close to Lys51 or Phe110 of HA. This simulation, however, provided no clear explanation for the mechanism of drug resistance due to the above amino acid mutations. The mechanism of the drug resistance of HA should be clarified for producing promising inhibitory compounds.

In this study, we performed computational analysis, screening to find candidate compounds, a cell-based antiviral assay, and synthesis of analogue compounds in the following manner: (1) Molecular dynamics (MD) simulations were carried out for the wild-type and three kinds of variants containing amino acid mutations responsible for drug resistance in order to clarify the mechanism. (2) A point for designing a potential inhibitor was deduced from the concept of minimizing the influence of the drug-resistance-related conformational change of HA. (3) An *in silico* screening was performed to find low-molecular-weight compounds showing inhibitory activity against HA, considering the above point and using the pharmacophore of stachyflin. (4) A cell-based assay was carried out to evaluate the inhibitory potencies of the compounds collected by the *in silico* screening. (5) Derivatives of the hit compounds found from the screening were synthesized, and their inhibitory activities were measured to elucidate the antiviral potency of the scaffold proposed in this work.

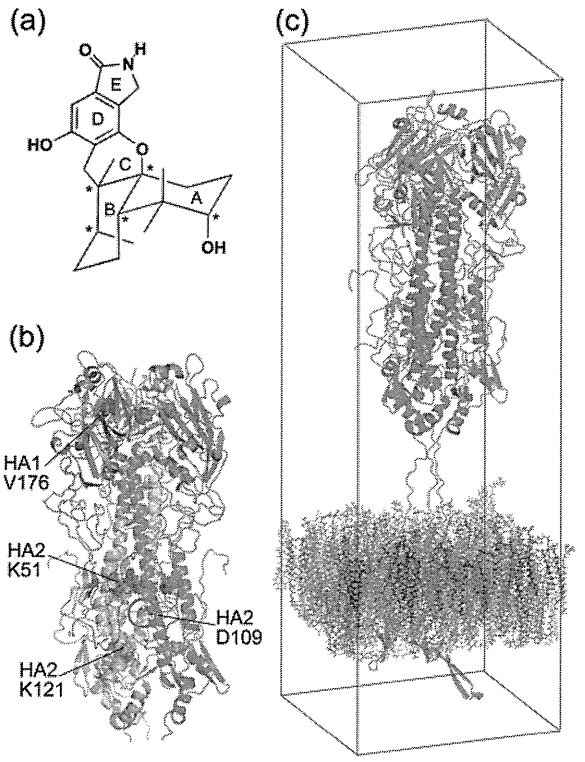

Figure 1. (a) Chemical structure of stachyflin. Stachyflin is composed of five complex rings and contains five chiral centers. The rings are labeled A−E, and chiral carbon atoms are marked by asterisks. (b) Structure of hemagglutinin in a trimer conformation. Spheres denote the residues introducing amino mutations in the respective mutants. The center residue targeted in the ligand docking simulation is indicated by a circle. (c) Calculation model of a complex of hemagglutinin trimer and lipid membrane. Hemagglutinin subunits HA1 and HA2 are colored blue and green, respectively. The membrane consists of 6 different kinds of lipid molecules, and its composition is presented in Supplementary Table S1. No water molecules or ions are shown for visual clarity.

RESULTS AND DISCUSSION

Structural Difference in HA between the Wild-Type and Mutants. MD simulation was carried out for 30 ns to obtain the probable protein structure of HA in a trimer form for the wild-type and three mutants, using the model system containing a trimeric hemagglutinin and viral lipid membrane as shown in Figure 1c. The respective mutants contain the resistant mutations K51R and K121E in HA2 for mutant 1, V176I in HA1 and K51R, K121E in HA2 for mutant 2, and V176I in HA1 and K51R in HA2 for mutant 3. Root mean square deviation (rmsd) relative to the structure after heating is shown in Supplementary Figure S1. The rmsd value for the wild-type (Figure S1a) was scarcely changed during 30 ns. Each of the rmsd curves for the mutants (Figures S1b−d) shows a

gradual increase up to 15 ns and seems to be almost constant after 20 ns. Plots of rmsd in Figure S1 were obtained from the coordinates of main chain atoms of the whole HA. The N-terminal domain of the HA1 subunit is so flexible that rmsd values are considerably large. Hence, rmsd values were calculated again with respect to the main chain atoms of only the HA2 subunit with excluding the C-terminal region, aa 176–222. The rmsd curves only for HA2 in Supplementary Figure S2 also became constant after 20 ns for every model. Accordingly, protein conformations for the respective models were judged to be equilibrated.

Principal component analysis (PCA) in Supplementary Figure S3 indicates that the trajectory structures for the last 5 ns are in a single conformation for every model. The equilibration of the simulation is also confirmed from these PCA plots. In order to extract the plausible protein structure, the averaged structure was obtained using 500 trajectory structures from the last 5 ns of MD simulation. The rmsd between each trajectory structure and the average structure was calculated, and then one trajectory structure with the smallest rmsd value was determined to be the plausible protein structure. At a glance, there is no prominent difference among the 4 models in terms of shape of the trimer, conformation of the HA1 and HA2 subunits, or position of helices. Although no significant apparent change is seen in the backbone of HA, there appears a notable difference in the location of side chains. The differences in the side chain will be responsible for the change in binding affinity and inhibitory activity of inhibitors.

Binding of an Inhibitor to HA. By means of docking simulation, an inhibitor, stachyflin, was bound to the HAs, using the respective plausible protein structures obtained by MD calculations. In the wild-type HA, stachyflin was bound near Asp109 of the HA2 subunit (Figure 2). Hydrophobic interactions were observed between the B ring of stachyflin and Phe37 of HA1, between the C ring of stachyflin and Phe110 of HA2, and between the D ring and Leu113. Hydrogen bonds were formed between the O atom on the D ring of stachyflin and the amino group of Asn114 in HA2 and between the O atom on the E ring and the amino group of Asn117.

In mutant 2, stachyflin was bound to a location similar to that of the wild-type (Supplementary Figure S4c), while the docking simulation showed binding of stachyflin at the central space among three helices of the HA2 trimer in mutants 1 and 3 (Figures S4b and d). Judging from the binding affinity evaluated by ASP score function (Supplementary Table S2), the binding of stachyflin to the wild-type HA is the most stable. All of the mutants showed notable decrease in binding affinity compared to that of the wild-type.

An amino acid mutation of K51R in HA2 commonly appeared in the three mutants, suggesting that K51R was the primary mutation for drug resistance. Other mutations, K121E and V176I, will enhance the resistance. All of these amino mutations are, however, distant from the stachyflin binding site. Our MD simulation clearly indicated that inner helices of HA2 subunit were rotated (Figure 3a). One of the three inner helices, chain D in nomenclature in PDB 1RD8, was rotated by 10.8° in mutant 1 and by 15.0° in mutant 2 compared to the wild-type (Figure 3b). The amino group on the side chain of Lys51 makes a strong hydrogen bond with the hydroxy group of Thr107 of HA2 (Figure 3c). Arg is also a positively charged amino acid residue, but the length of the side chain is longer than that of Lys. When Lys is converted into Arg, the side chain

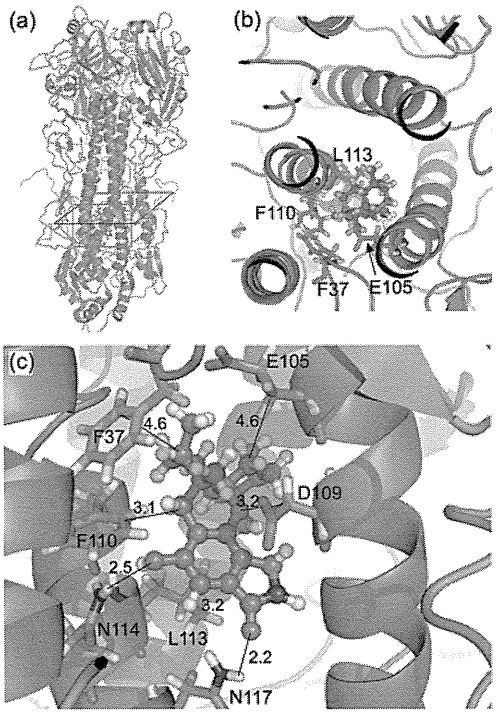

Figure 2. (a) Complex structure of stachyflin and hemagglutinin obtained by the ligand docking simulation. (b) Binding site of stachyflin viewed in a plane perpendicular to the helices of the HA2 subunit. (c) Binding mode of stachyflin, shown in a magnified view of the area indicated by a red frame in panel a. Stachyflin is bound to the space between two helices of HA2 subunit, making strong interaction with side chains of Asp109, Phe110, and Leu113. The interaction distances are in Å.

of the residue at codon 51 expands and pushes T107. The side chain of Thr107 serves as a lever to rotate the helix. The position of the side chain of Asp109 is largely deviated from that of the wild-type because of the closeness to Thr107. Lys121 has a strong interaction with the carboxy group of Asp18 of the HA1 subunit. When Lys is converted into Glu in the K121E mutation, the side chain of Glu121 and Asp18 of HA1 causes repulsion to increase the distance between them. This repulsion assists the helix rotation, and the deviation of Leu113 and Asn114 from the wild-type will be enhanced because of the closeness to Glu121. To monitor the helix rotation, the angle between the line connecting the Cα and Cβ atoms of Asp109 on the inner helix chain D and the line connecting the Asp109 Cα atom on chain D and the Phe110 Cα atom on another inner helix chain B was measured through the simulation as shown in Supplementary Figure S5. A significant angle change was observed after 10 ns for every model. The distances between the Nζ atom of Lys51 (or Cζ in K51R) of HA2 and the Oγ atom of Thr107 of HA2 and also between the Nζ atom of Lys121 (or Cδ in K121E) of HA2 and Cγ of Asp18 of HA1 were monitored as shown in Supplementary Figure S6. Because HA is a trimer and there exist three HA1 and three HA2 subunits in the calculation models, three combinations of those interatomic distances were measured through the simulation. The distance plots in Figure S6 indicate that the interaction between the residues at codon 51 and codon 107 is quite stable in the wild-type HA. In contrast, some of these distances occasionally increased in the mutants. The distance between the residues at codon 121 of HA2 and at codon 18 of HA1 ceaselessly fluctuated in all